



THESIS APPROVAL SHEET

Title of Thesis: Design Optimization of a Wind Tunnel Force Balance Using Stepwise Response Surface Method

Name of Candidate: Thomas Chaisson

Master of Science 2021

Graduate Program: Mechanical Engineering

Thesis and Abstract Approved:

Soobum Lee

Soobum Lee

Associate Professor

Mechanical Engineering

7/31/2021 | 9:38:22 AM EDT

NOTE: *The Approval Sheet with the original signature must accompany the thesis or dissertation. No terminal punctuation is to be used.

Abstract

Title of Document: Design Optimization of a Wind Tunnel Force Balance
Using Stepwise Response Surface Method

Thomas Chaisson

Directed by: Dr. Soobum Lee, Dr. Devin Burns

A force balance is a device utilized in wind tunnels in order to measure the forces being applied to a body during a wind tunnel test. The balance is equipped with strain gauges that measure structural deformations for evaluation of the forces and moments being applied to the body. The force balance is required to have structural safety under a large roll moment, due to design changes with the testing apparatus. The balance must be optimized to allow for this increased roll moment while guaranteeing the balance will not fail and the gauges within the balance will generate an acceptable gauge reading.

The finite element simulation-based design optimization is studied in this thesis. Firstly, a finite element (FE) model of the force balance was created. To ensure the model accuracy of the force balance, a comparison of the stress values and the gauge readings was conducted while the balance experienced rated loads. Second, two response surface method (RSM) trials were run using three sampling techniques: Central Composite Circumscribed (CCC), Central Composite Face-centered (CCF), and Box-Behnken (BB). The first trial is a broad sampling centered around the original dimensions. The results of the first trial led to the second trial, which consisted of narrow sampling with a center point closer to the optimal point than the first trial. The data from these trials was then utilized in a final regression, in which a final quadratic model was generated

to find a further optimized point. The result of this study shows the force balance design changes to decrease stress values with a greatly increased roll moment and provides satisfactory gauge readings. This thesis successfully demonstrated the benefit of the stepwise RSM that can achieve optimal design using limited number FE analysis.

Design Optimization of a Wind Tunnel Force Balance
Using Stepwise Response Surface Method

By

Thomas Chaisson

Thesis submitted to the Faculty of the Graduate School of the
University of Maryland, Baltimore County, in partial fulfillment
of the requirements for the degree of

Master of Science

2021

Dedication

For my family, for I could not accomplish what I have without their unwavering support.

Acknowledgements

Firstly, I owe my greatest thanks to Dr. Soobum Lee, for if not for his guidance and opportunity, I would not have gotten to where I am today. He invited me to work alongside himself, Dr. Devin Burns, and Dr. Peter Parker, whom I both owe a great amount of gratitude towards, at NASA Langley Research Center, who have all provided me with knowledge and help that I will take with me on my next venture. Thank you.

I also owe gratitude to Dr. Jamie Gurganus, Dr. Anthony Farquhar, and Dr. Marc Zupan, not only for serving on my thesis committee, but for assisting me throughout my undergraduate career. Their help led me to pursue higher education, and I appreciate everything they have done for me.

Finally, I owe thanks to the NASA Langley Research Center for giving me the opportunity to not only work with them, but also allowing me to incorporate my work into a thesis. This work is supported by NASA internship contract numbers 17947 (Fall 2020) and 18994 (Spring 2021).

Table of Contents

1.	Introduction	1
1.1	Force balance	1
1.2	Response Surface Methodology.....	5
1.3	Objective	6
2.	Design layout and calibration of the finite element model.....	7
2.1	Design layout of the force balance.....	7
2.1.1	Assembly of the force balance.....	7
2.1.2	Exterior components.....	8
2.1.3	Interior components	11
2.2	Calibration of the force balance.....	17
2.2.1	Stress analysis.....	18
2.2.2	Strain gauge reading analysis.....	26
2.2.3	Discrepancy analysis on stress and strain gauge reading.....	28
2.3	Maximum stress analysis of force balance.....	32
2.4	Balance response by increased roll moment	35
3.	Design optimization of balance	37
3.1	Variables	37
3.2	Sampling for Response Surface Method.....	39
3.3	Response Surface Modeling.....	42
3.3.1	Trial 1 – Initial Broad Sampling.....	47
3.3.2	Trial 2 – Focused Sampling.....	55
3.3.3	Final Regression – sum of least squares error	64
4.	Conclusion and future work.....	67

4.1	Conclusion	67
4.2	Future work	68
5.	References	71

List of Tables

Table 1: Force Balance Rated Loads [26].....	5
Table 2: Stress values in force balance components with theoretical calculations, individual FEA, and assembly FEA (ksi).....	26
Table 3: Calibration vs. FEA gauge reading results	28
Table 4: Stress in normal force element with varied roll cage flexure hinge thicknesses	29
Table 5: Stress values in force balance components with theoretical calculations, individual FEA, and assembly FEA with updated roll cage (ksi)	31
Table 6: Calibration vs. FEA gauge reading results with updated roll cage	31
Table 7: Maximum stress analysis of force balance	33
Table 8: CCC, CCF, and BB sampling example	42
Table 9: Weight values of w_1 and w_2	46
Table 10: Trial 1 CCC sampling data.....	48
Table 11: Trial 1 CCF sampling data	48
Table 12: Trial 1 BB sampling data	49
Table 13: Trial 1 model coefficient values.....	50
Table 14: Trial 1 CCC optimized points data.....	51
Table 15: Trial 1 – CCC optimized point output comparison	51
Table 16: Trial 1 CCF optimized points data	52
Table 17: Trial 1 – CCF optimized point output comparison	53
Table 18: Trial 1 BB optimized points data	53
Table 19: Trial 1 – BB optimized point output comparison.....	53
Table 20: Maximum stress values at varying x_2 dimensions.....	55
Table 23: Trial 2 CCC sampling data.....	56
Table 24: Trial 2 CCF sampling data	57

Table 25: Trial 2 BB sampling data	57
Table 26: Trial 2 model coefficient values.....	58
Table 27: Trial 2 CCC optimized points data.....	58
Table 28: Trial 2 – CCC optimized point output comparison	59
Table 29: Trial 2 CCF optimized points data	60
Table 30: Trial 2 – CCF optimized point output comparison	60
Table 31: Trial 2 BB optimized points data	61
Table 32: Trial 2 – BB optimized point output comparison.....	61
Table 33: Trial 2 best points stress and gauge reading FEA values	63
Table 34: Regression output data	65
Table 35: Regression coefficients.....	65
Table 36: Regression optimized point output comparison	66
Table 37: Optimized variables by the final regression model.....	67

List of Figures

Figure 1: Force balance utilized within model aircraft within wind tunnel [3]	2
Figure 2: Multi-piece force balance patent [4]	2
Figure 3: Roll cage flexure after failure [25].....	4
Figure 4: CAD geometry of assembled force balance.....	8
Figure 5: CAD geometry of cross-sectional view of force balance with exterior components. (a) Inner rod. (b) Outer sleeve	10
Figure 6: CAD geometry of cross-sectional view of force balance with individual components and gauge locations. (a) Normal force element. (b) Side force element. (c) Roll cage. (d) Axial/chord force member.	14
Figure 7: Example roll cage with gauge placements	16
Figure 8: CAD geometry of roll cage cross-sectional view	16
Figure 9: FE mesh representation. (a) Full meshed force balance assembly. (b) Close view of meshed normal force element flexure. (c) Close view of meshed roll cage flexure.....	18
Figure 10: FEA results of normal force element undergoing 3000lb rated load. (a) y- directional stress contour. (b) deformation mode under compression load (black and red indicate each member, solid and dashed lines indicate before and after deformation). (c) deformed shape of CAD model.....	20
Figure 11: Representation of side force element and chord force element flexures and variables x and s [26]	22
Figure 12: FEA results of side force element undergoing 1500lb rated load – x-directional contour.....	23
Figure 13: FEA results of chord force element undergoing 600lb rated load – z-directional contour.....	24
Figure 14: FEA results of roll cage undergoing 6000in-lb rated moment – Shear contour	25
Figure 15: Wheatstone bridge diagram	26
Figure 16: Roll cage flexure location	30
Figure 17: Enhanced view of roll cage flexure. (a) Original roll cage flexure dimensions. (b) 80% reduction in hinge thickness roll cage flexure	30

Figure 18: FEA of normal force element in assembly with axial/roll/pitch/yaw combined load – von Mises contour	34
Figure 19: Cross-sectional view of force balance with location of maximum stress under combined rated load	35
Figure 20: FEA of roll cage flexure in assembly with normal/side/axial/roll combined load – von Mises contour	35
Figure 21: Cross-sectional view of force balance with location of maximum stress	36
Figure 22: Roll cage flexure under 20,000in-lb moment – von Mises contour.....	36
Figure 23: Roll cage flexure variables, hole cutout diameter (blue) and hinge thickness (yellow)	38
Figure 24: Roll cage gauge location thickness variable, referenced at the outer surface.....	39
Figure 25: A 3-dimensional representation of a CCC sampling	40
Figure 26: A 3-dimensional representation of a CCF sampling	40
Figure 27: A 3-dimensional representation of a BB sampling	41
Figure 28: Design process flow chart.....	43
Figure 29: Trial 1 normalized stress and gauge reading plot	54
Figure 30: Trial 2 normalized stress and gauge reading plot	62
Figure 31: Stress and gauge reading values for Trial 1 and 2 BB sampling	63
Figure 32: Forward end of roll cage flexures. (a) Original roll cage flexures. (b) Updated roll cage flexures	67
Figure 33: Cross-sectional view of roll cage gauge location. (a) Original roll cage gauge location. (b) Updated roll cage gauge location.	68
Figure 34: Radial distance between hole cutouts in roll cage flexure (blue). Cutout thickness in roll cage flexure (yellow).....	69

List of Nomenclature

α	coefficients related to final regression
A	cross-sectional area of flexure
β	coefficients related to RSM regression
b	flexure width
C	distance from neutral axis to end of flexure
D	diameter
d	distance from idealized point
ε	gauge reading model
ε_0	center point gauge reading
ε_i	strain data
f	normalized stress and gauge reading function
I	moment of inertia
K	gauge factor
L	number of sampled points
M	moment flexure experiences around center
N	number of variables
ω	weighted regression values
P	applied load
RSS	sum of least squares error
σ	stress
σ_0	center point stress
τ	shear stress
t	flexure thickness
V_r	Wheatstone bridge gauge reading output
W	weighted regression matrix
w	model weighted values

x	variables
x_a	offset distance from the magnitude of the redundant moment
y	model output

1. Introduction

1.1 Force balance

Force balances are devices that carry strain gauges that read strains in the axial directions in order to determine the forces and moments acting on a body, primarily used in wind tunnels. In general, force balances can be categorized into two groups: single piece balances and multi-piece balances. Single piece balances benefit from not having error due to fasteners and tolerance issues between components but are often more difficult to produce and require manufacturing techniques like additive manufacturing [1] or wire EDM [2]. This study will focus on a multi-piece balance.

Multi-piece balances have a configuration containing six internal components with two outside housing components. The internal components consist of two normal force elements, two side elements, an axial or chord force member, and a roll cage. The two outer components which house the inner components are the inner rod and the outer sleeve. Forces are applied to the outer sleeve, which then transfer forces into the inner components. The force is transferred then through the inner components, where the deformations are read and the strains calculated, then to the inner rod. The inner rod is the non-metric piece of the assembly, as it is the fixed piece. An example of the balance working within a model aircraft is shown in Figure 1 [3]. A patent of the multi-piece balance can be shown in Figure 2 [4]. A detailed working principle is found in Section 2.

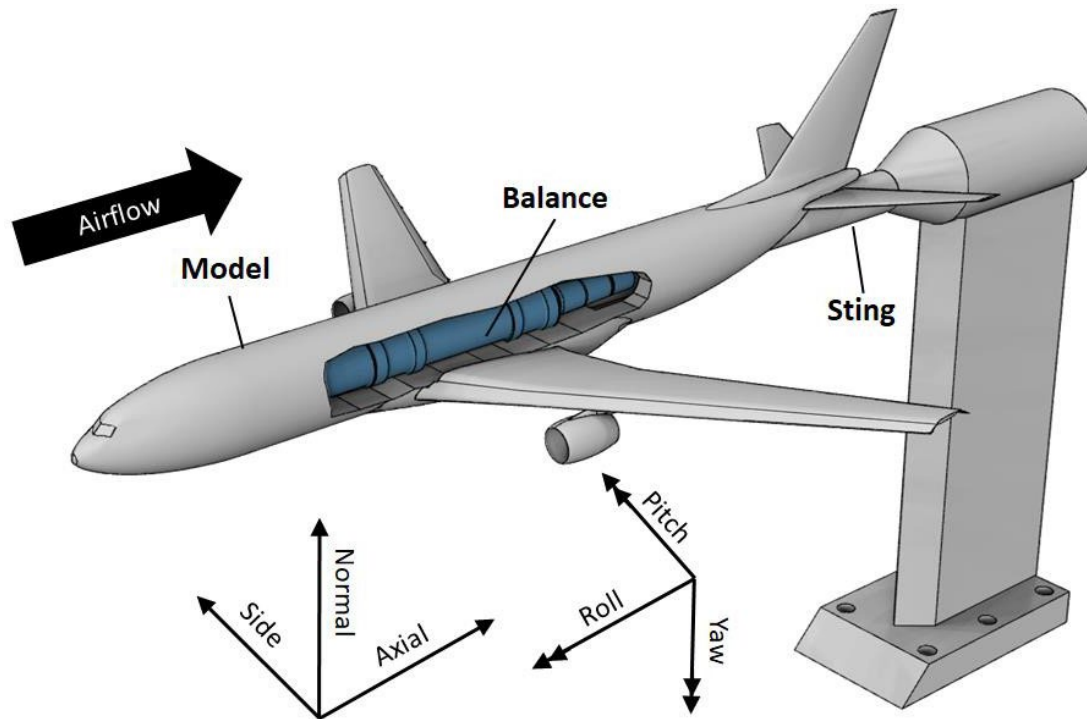


Figure 1: Force balance utilized within model aircraft within wind tunnel [3]

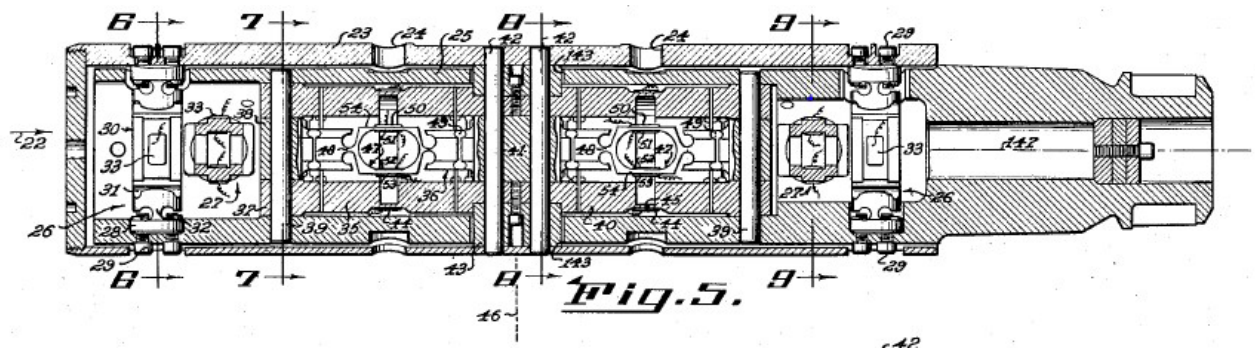


Figure 2: Multi-piece force balance patent [4]

Force balances have been subjected to many changes to fit a wide variety of needs. Firstly, it is found that these balances can measure forces applied to a body [5], [6]. Certain balances are designed to measure specific forces only, like a balance to measure lift and drag [7] and a balance that only measures the 3 axial directions of force [8]. Because certain aeronautic situations require aircraft to go through extremes of speed and temperature, balances are designed to assist in the design and testing process of these aircraft. Certain balances were designed to handle supersonic [9] and hypersonic flow [10], [11], [12], as well as able to read

forces in areas where the Reynold's number is significantly lower than normal conditions [13], [14]. Extreme cold temperatures are also considered when designing aircraft to fly high in the atmosphere, so a normal force balance must be calibrated correctly to negate the thermal compression the balance experiences [15]. Finally, it has been found that balances have been designed to measure both sudden impulses [16] and forces over time to get a frequency reading [17], [18]. The balance has also been used to measure force frequency that a high-rise building experiences, which is completed by placing a highly accurate force balance at the base of a tall building to measure the base forces and overturning moments acting on the building [19]. Balances have also been used not only to measure forces on a body, but to compare the efficiencies of engines [20].

Alongside all the various tasks force balances have been modified to fit, improvements have been made to assist the general efficiency and performance of the balance. How the balance is mounted has a major impact on errors within the balance. It was found that mechanical decoupling helps reduce these errors [21], and certain configurations of balances can reduce cross-axis coupling, such as a symmetric configuration within the balance, center-thickened beams, and constraining the beams in a fixed-fixed manner. [22]. These configurations are seen in the balance used in this thesis, shown later in Section 2.1.1. To further reduce cross-axis coupling, the balance can be mounted magnetically to reduce any contact on the non-metric ends of the balance [23]. Finally, for large scale balances, a lightweight modular model was created for ease of use and transportation [24].

Although work has been done to both learn about and improve force balances, much is still unknown about various balances. For example, the Bennett document [25] focuses on an older model of a force balance created in the 1960's. This balance was recreated in a CAD software

and tested at its rated loads alongside the physical balance. This article found that the balance failed at certain rated loads, as shown in Figure 3 [25] where the roll cage flexures failed, causing a crack between the hole cutouts.

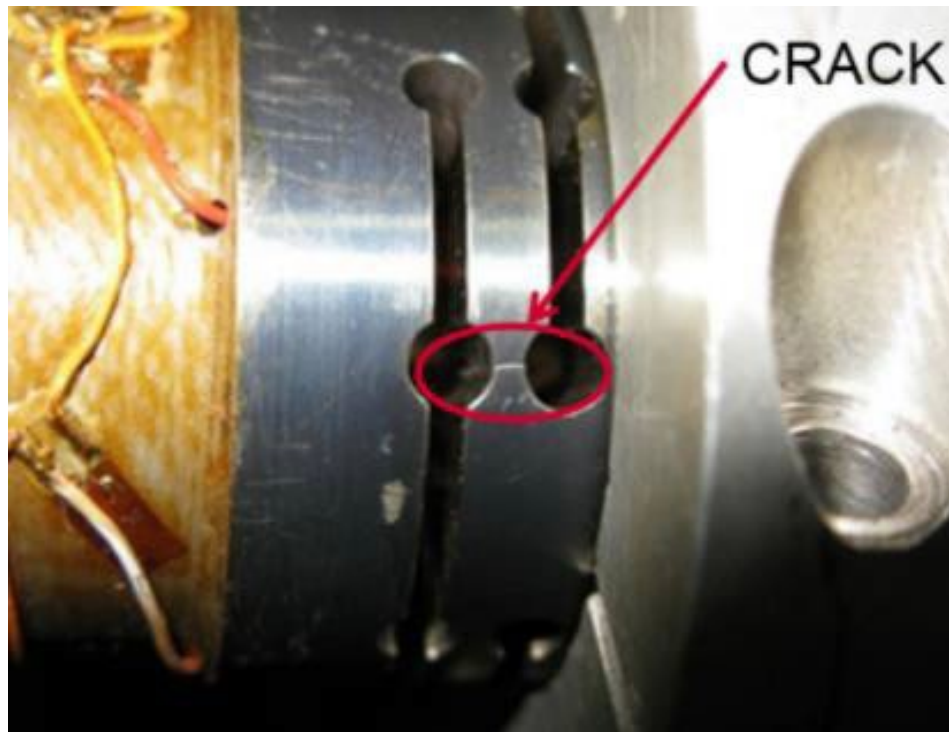


Figure 3: Roll cage flexure after failure [25]

This study will focus on a balance that was created in the same time period as the one in Bennett's study. This balance is an older force balance, but it is still used and is the best assembled balance for a specific test on an aircraft. The balance will have to be recreated as a finite element model and tested with its rated loads to ensure its computational accuracy. The rated loads for the balance focused on in this study are listed in Table 1 [26]. Then, the balance design modification study will be followed to avoid structural failure like the roll cage crack in Figure 3.

Table 1: Force Balance Rated Loads [26]

Component	Total Rated Load	Individual Component Rated Load
Normal Force	3000 lb	1500 lb
Side Force	1500 lb	750 lb
Chord Force	600 lb	600 lb
Rolling Moment	6000 lb-in	6000 lb-in
Pitch Moment	22500 lb-in	22500 lb-in
Yaw Moment	9750 lb-in	9750 lb-in

1.2 Response Surface Methodology

To achieve an optimized design change, response surface methodology (RSM) will be utilized. RSM was selected for its ability to allow for the use of multiple variables to create a numerical representation of a model [27], as well as allow the creation of interpolation functions to represent an otherwise complicated and difficult to find function that should be optimized [28], [29]. RSM will assist in displaying a non-linear multi-dimensional model [30], [31] that also allows for a non-linear relationship for further variable correlation [32], [33]. Finally, an adaptive trial-based system is beneficial in this case to take the optimized point of one trial and move that as the center of the next, which RSM is able to do [34], [35] and this thesis utilized.

Response surface methodology can be utilized in this case for reliability-based design optimization (RBDO). RBDO is becoming more useful for a varied number of optimization problems throughout the engineering design field. This method allows for the use of unknowns that will assist in the creation of a model that will abide by setting design variables [36], [37]. RBDO may utilize a number of different techniques: a gradient approach to increase the effectiveness of RBDO in extreme nonlinearities [38], sequential optimization to solve for quadratic models [39], [40], and single loop approaches to assist in long-term time-based optimization problems [41], [42]. The single loop approach focuses on approximating the

reliability constraint of a system to estimate how long the model will remain efficient or run without failure [43]. Specific models have been created to handle RBDO as well, like the Kriging model, used to improve the computational efficiency by interpolating values through a Gaussian process governed by previous covariances [44], [45]. Other models involve a hybrid of various techniques to increase efficiency, such as combining the Monte Carlo Simulation (MCS) with a hybrid Artificial Neural Network (ANN) based Whale Optimization Algorithm (WOA) [46]. RBDO is utilized for a number of reasons, the first being that it allows for simulating and optimizing a scenario that would either be too costly [47], [48], would be too unsafe [49] or would be unfeasible [50] to run a physical model. This method of optimization creates a theoretical model of the desired system. RBDO also relies on estimation based on raw data from the physical system to create its theoretical model [51], [52]. If a system is extremely complex, certain RBDO models are able to create realistic models of the system by utilizing random and interval uncertainties [53], [54]. This includes systems where the design parameters may change, creating uncertainties, such as optimizing the joints of a lower extremity exoskeleton, who's dimensions will change based on the subject utilizing the device [55]. Finally, RBDO allows for a resampling of data after an initial model generation, which will allow the system to calibrate a new system more accurately than before [56]. This resampling is utilized during the optimization process.

1.3 Objective

The first objective of this study is to create a working finite element model of the force balance assembly. The model must be calibrated to ensure it depicts the actual force balance effectively. The second objective is to obtain the optimal design of the force balance that has an acceptable stress measure by the increased load (roll moment) while maintaining satisfactory

gauge readings. The finite element model of the force balance will be utilized to evaluate the stress and strain out of the increased roll moment from 6000in-lb to 20,000in-lb. The balance's outer dimensions must stay the same, as the tool must be able to fit in the same apparatus it is currently used in. There exist two design requirements regarding the maximum stress not exceeding its threshold value and the output gauge reading to be close to its target [57], which will be described in detail in this thesis.

2. Design layout and calibration of the finite element model

2.1 Design layout of the force balance

To conduct the optimization of the force balance subject to the rated roll moment, a finite element model must be created. However, there does not exist a drawing or model of this piece, so building the model required information from a stress analysis [26]. This document contained theoretical stress and strain calculations for sections of the interior components, and all available dimensions found in these calculations were used to attempt a recreation of the force balance. All missing dimensions were inferred through using known dimensions and comparing those to general drawings of this force balance.

2.1.1 Assembly of the force balance

The complete force balance is made by assembling multiple components as listed in the following subsections. In practice, this balance will be placed inside a model aircraft within a wind tunnel, fixed at both ends. The balance provides the forces and moments in all axial directions. Figure 4 shows the CAD geometry of the completed assembly. Each component

within the force balance is manufactured from Carpenter 455 stainless steel [26]. The model was designed and simulated completely using Creo 4.0 [58].



Figure 4: CAD geometry of assembled force balance

2.1.2 Exterior components

The force balance has 2 exterior components: the inner rod which houses all components and the outer sleeve which is where forces are applied. The inner rod has two non-metric fixed ends, which is an uncommon trait in force balances. Figure 5 displays a cross-sectional view of the force balance that shows the locations of the exterior components, as well as an exterior view of each exterior component: (a) inner rod, (b) outer sleeve.

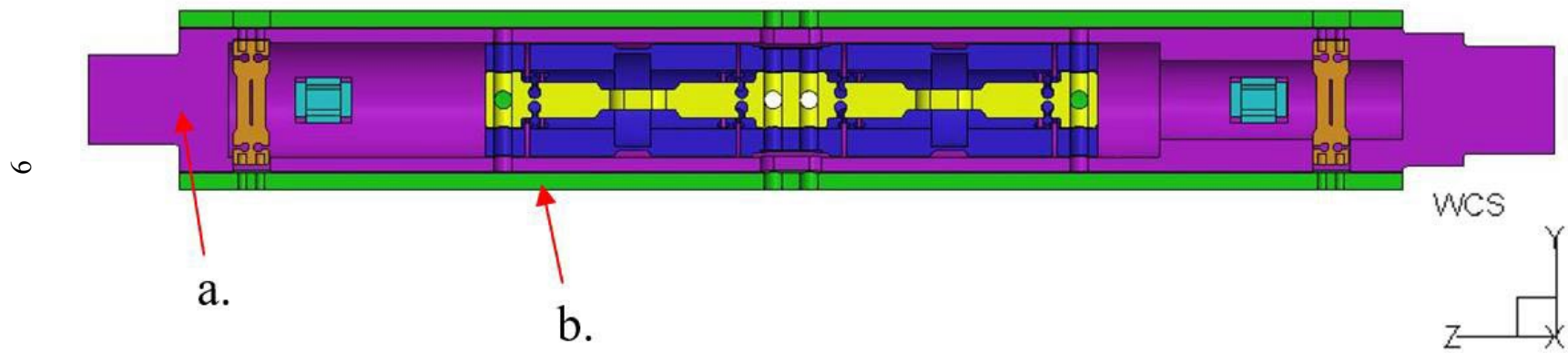


Figure 5: CAD geometry of cross-sectional view of force balance with exterior components. (to be continued)

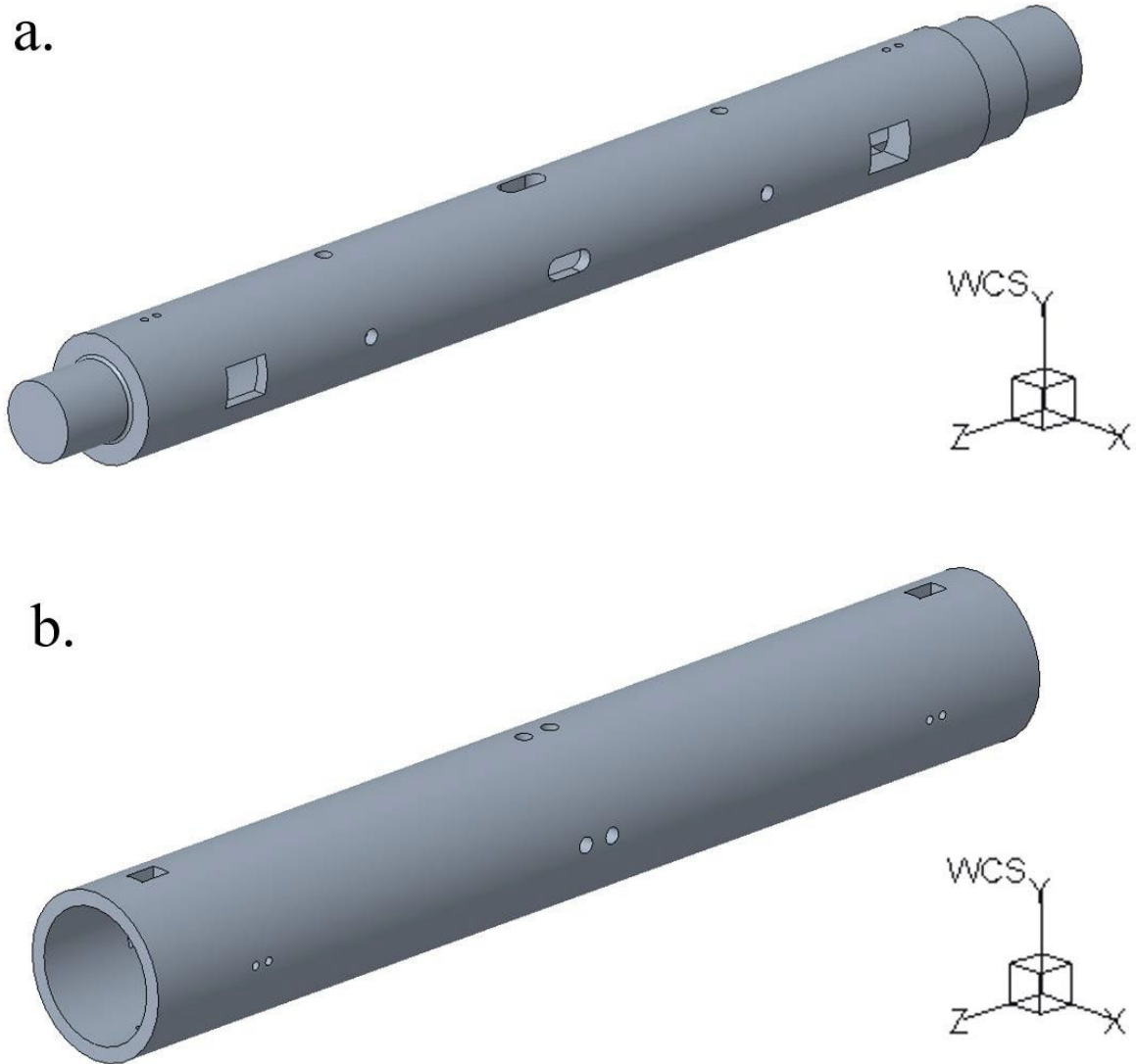


Figure 5: CAD geometry of cross-sectional view of force balance with exterior components. (a) Inner rod. (b) Outer sleeve.

The inner rod in Figure 5(a) contains enlarged holes in the center of the piece to allow fasteners to connect between the outer sleeve and the several interior components (Section 2.1.3) with no interference from the inner rod. The outer sleeve in Figure 5(b) is a simple, cylindrical piece that acts as the medium between forces applied and the inner components. Both ends of the inner rod are fixed.

2.1.3 Interior components

There are a total of four unique interior components within the force balance. Figure 6 displays a cross-sectional view of the force balance to distinguish parts and their locations within the balance. Each internal component displayed in Figure 6 is: (a) normal force element, (b) side force element, (c) roll cage, (d) axial/chord force member. The normal and side force elements are fixed on both the forward and aft sections of the inner rod. The roll cage and chord force member are fixed to the inner rod at the mounting holes a few inches away from the center. Figure 6 also displays the locations of gauges on each component and the orientation of the gauges, as dictated by red squares (location) and black lines (orientation).

The outer sleeve is connected to the roll cage and chord force member through the fastening holes in the center. One end of the side and normal force elements is fastened to the outer sleeve as well.

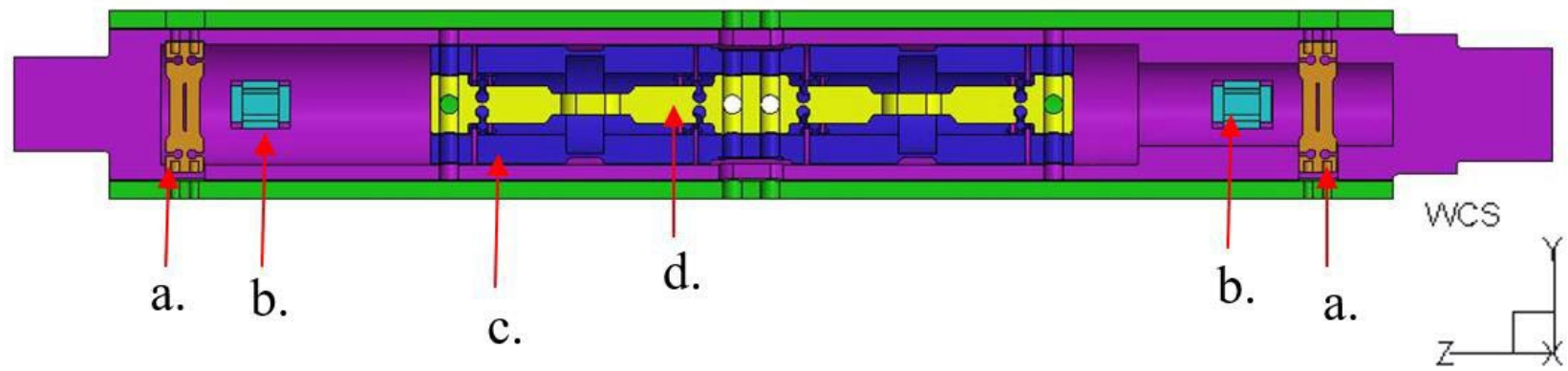


Figure 6: CAD geometry of cross-sectional view of force balance with individual components and gauge locations (to be continued)

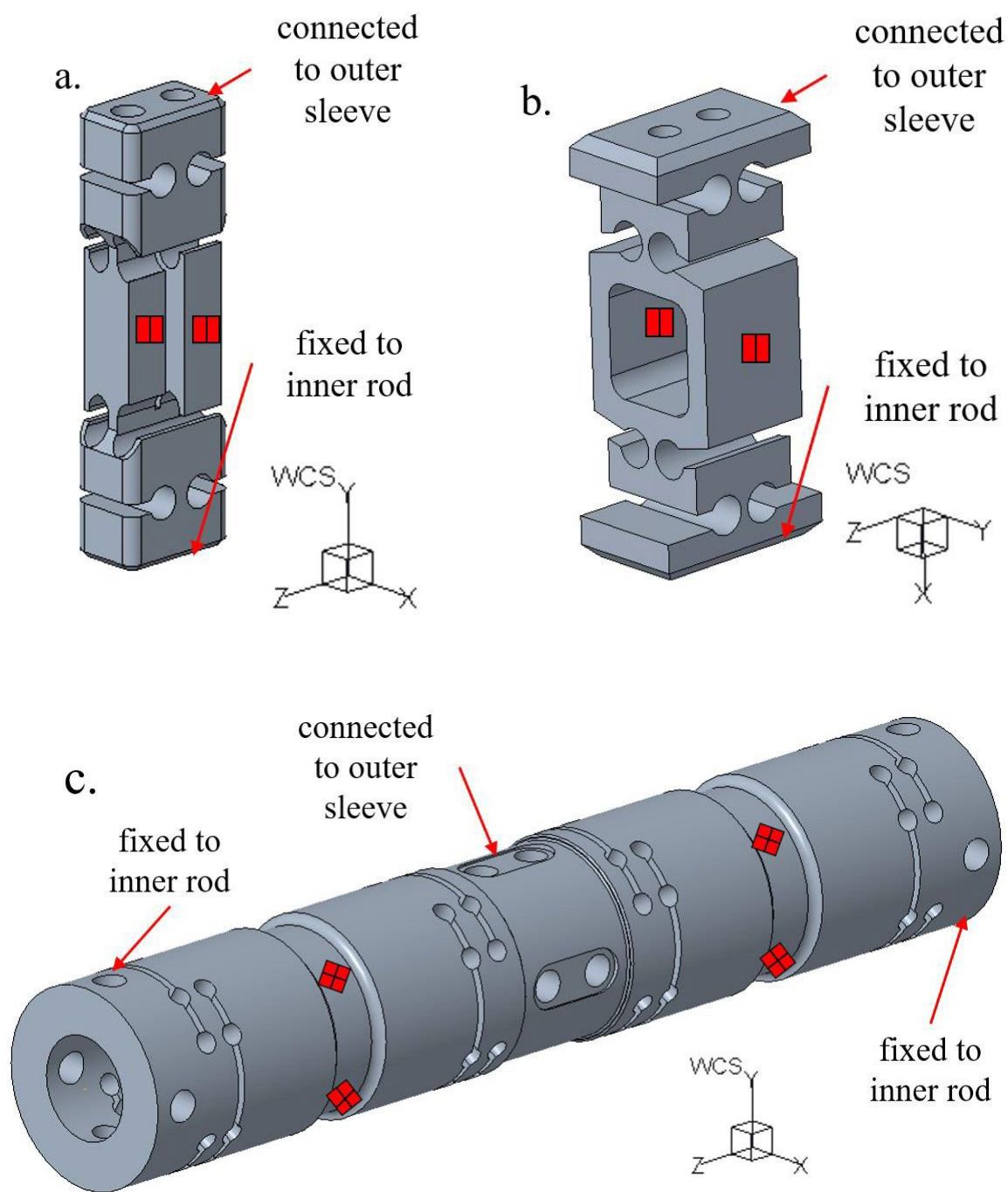


Figure 6 (continued)

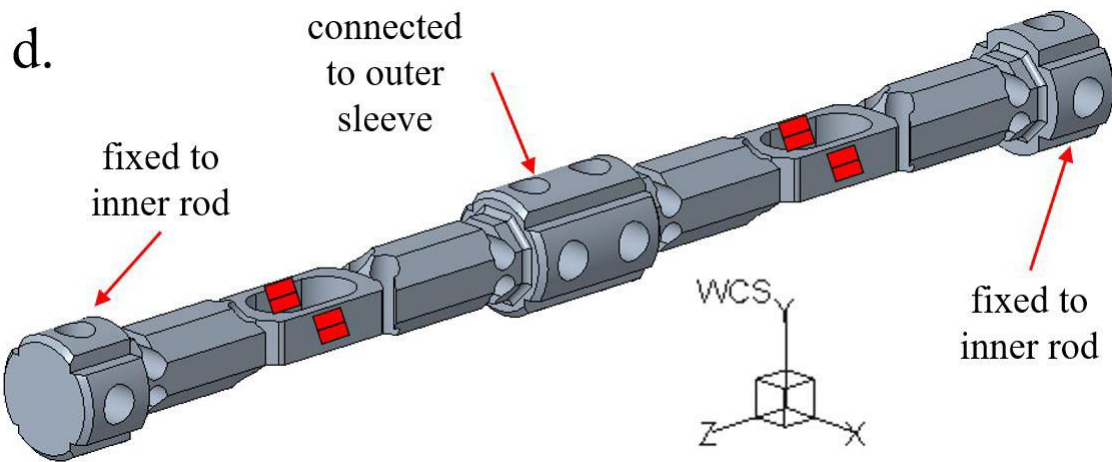


Figure 6: CAD geometry of cross-sectional view of force balance with individual components and gauge locations. (a) Normal force element. (b) Side force element. (c) Roll cage. (d) Axial/chord force member.

The normal force element is the component on the forward and aft sections of the force balance shown in Figure 6(a). The normal force element is a symmetrical piece with two flexures that allow for deformation, which is where the gauges are placed. The gauges for the normal force element would be placed on the center of both sides of each flexure in the center of the piece, as shown by the red squares located on the piece. These pieces will measure the deflections in the normal direction in the y -axis direction. Having one piece in the forward section and one in the aft section allows this balance to measure not only the normal forces acting on the system but also the pitch moment about the x -axis. One end of the element would be fixed to the inner rod and be fixed, whereas the other end would be connected to the outer sleeve, where forces would be transferred from.

The second component is the side force element, which is the element shown in the forward and aft sections of Figure 6(b). The flexures differ from the normal force element in terms of the rated loads as shown in Table 1: the normal rated load is 3000lb, whereas the side rated load is 1500lb. The balance utilizes the same gauges throughout, and these gauges are set to measure

around 500-1200 μ strain. Therefore, the normal force element must remain stiffer than the side force element and was given a stiffer gauge section flexure. The gauges for this component are placed on the inside and outside of the center of the middle flexure, in order to create a complete bridge, as shown in Figure 6(b) by the red squares. Similar to the normal force element, there is a single side force element in the forward and aft sections. This allows this balance to measure both side force in the x -axis direction and yaw moment about the y -axis.

The third internal component is the roll cage, which lies in the center of the force balance, shown in Figure 6(c). The ends of the roll cage are fastened to the inner rod, leaving the ends fixed. The center is then fastened to the outer sleeve to allow for force to be transferred through the outer sleeve, into the roll cage and the inner rod. The roll cage is the only component that does not measure strain in one axial direction, but does measure the shear strain and figure out the roll moment about the z -axis. There are two gauges placed on each of the thinner sections of the roll cage, which appear on the forward and aft sides of the force balance. The gauges are placed such that they are not in line with the fastening holes, as displayed by the red squares in Figure 6(c). Figure 7 shows a force balance similar to the one focused in this study with gauges to display the placement (circles in the picture). The gauges are rotated at a 45° angle to read the shear strain in angled directions which is used to solve for the roll moment.

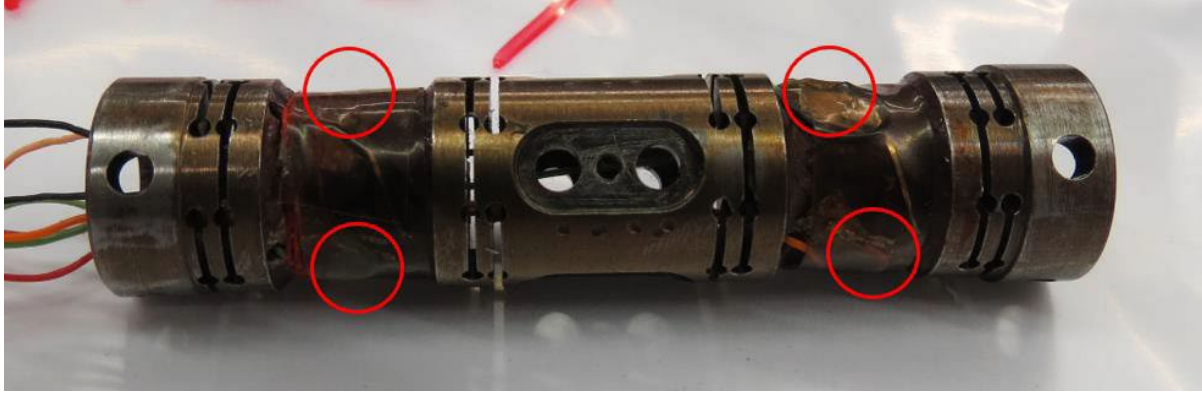


Figure 7: Example roll cage with gauge placements

The cross-sectional view of the roll cage in Figure 8 shows that the roll cage has variable diameter throughout the inside. The area where the gauges are placed has a larger inner diameter than the rest of the roll cage. This is because the gauges must read values around 500-1200 μ strain, therefore the gauge section thickness must accommodate that change.

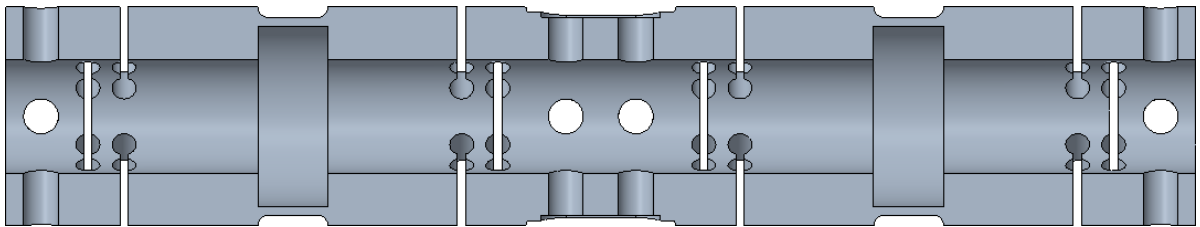


Figure 8: CAD geometry of roll cage cross-sectional view

The final internal component of the assembly is the axial/chord force member as shown in Figure 6(d). The chord force member shares a similarly shaped gauge flexure and the rated load is relatively smaller than other components at 600lb. This flexure allows the gauges to read values of strain between 500-1200 μ . The gauges are located as shown in Figure 6(d). as dictated by the red squares. The chord force member lies inside the roll cage, and its forward and aft ends are fastened to the inner rod and are therefore fixed. The center is fastened to the outer sleeve to allow for forces to transfer from the outer sleeve to the inner rod.

2.2 Calibration of the force balance

To ensure this model could be used to accurately represent the true balance's response, calibration had to be completed. The FEM was tested at its rated loads and the stress and gauge readings were evaluated. These values were then compared to theoretical and experimental data. The meshed FE model used in this thesis is shown in Figure 9(a). The mesh consists of 158,377 second order tetrahedral entities throughout the force balance. Closer visuals of the mesh density are available in Figure 9(b) for one of the meshed normal force element flexures and Figure 9(c) for the meshed roll cage flexure.

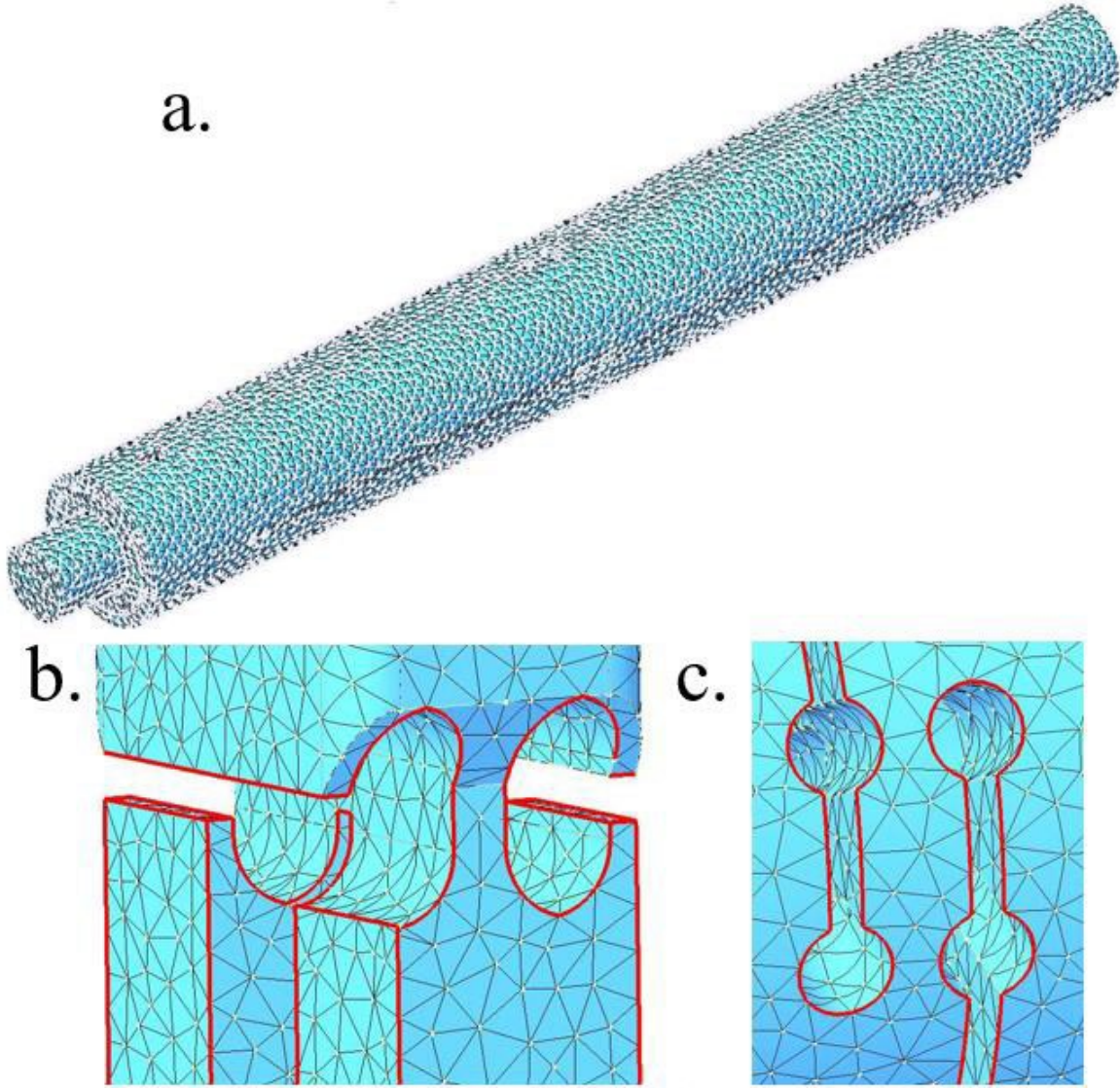


Figure 9: FE mesh representation. (a) Full meshed force balance assembly. (b) Close view of meshed normal force element flexure. (c) Close view of meshed roll cage flexure.

2.2.1 Stress analysis

The components were tested individually using FEM under their rated loads and extended to an assembly level. This was done to compare directly to theoretical values found in the stress analysis document [26]. This component is designed by placing two identical beams side by side so that they experience compressive and bending loadings simultaneously, as shown in Figure

10. The axial and bending stress for the element are shown in equations 1 and 2. The normal force element measures stress in the y -direction.

$$\sigma_{axial} = \frac{P}{bt} \quad (1)$$

$$\sigma_{bending} = \frac{6Pe}{bt^2} \quad (2)$$

where P is the load on one flexure, b and t are the width and thickness of one flexure, and e is the distance between the offset centers of the two flexures. The stress on the gauge section can be found by adding both stresses as in equation 3.

$$\sigma_{total} = \sigma_a + \sigma_b \quad (3)$$

The normal force element was subjected to a 1500lb compression force applied to the one end of the element, and the piece was fixed at the opposite end. Figure 10(a) displays the results of the FEM, and Figure 10(b) displays the deformation mode under a compression load, where black is the front member, red is the back member, the X locations are gauge locations, and the dashed line represents the deformation. The actual deformation of the CAD model is displayed in Figure 10(c).

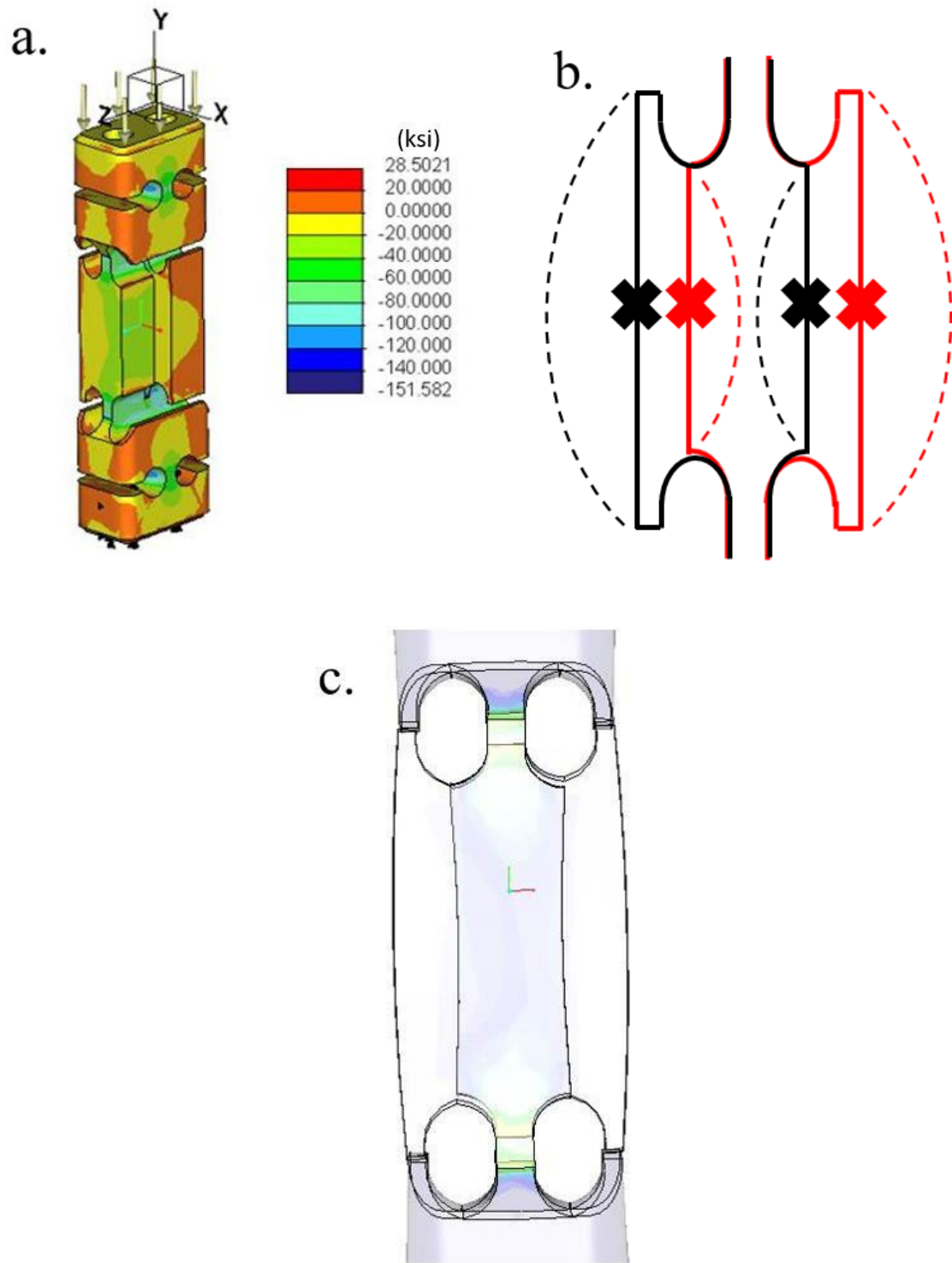


Figure 10: FEA results of normal force element undergoing 3000lb rated load. (a) y-directional stress contour. (b) deformation mode under compression load (black and red indicate each member, solid and dashed lines indicate before and after deformation). (c) deformed shape of CAD model.

The side force element and the chord force members share similar gauge flexure sections, and the axial and bending stress calculations are as follows in equations 4 and 5.

$$\sigma_{axial} = \frac{P}{2A} \quad (4)$$

$$\sigma_{bending} = \frac{MC}{I} \quad (5)$$

where P is the rated load for each component, A is the cross-sectional area of one side of the flexure, M is the moment the flexure experiences about its center, C is half the thickness of the flexure, and I is the moment of inertia. M is given as equation 6:

$$M = P(x - x_a) \quad (6)$$

where x is defined as the distance from the horizontal neutral axis of the component to the middle of the flexure, as shown in Figure 11. The variable s , which is the distance from the vertical neutral axis, is shown in Figure 11.

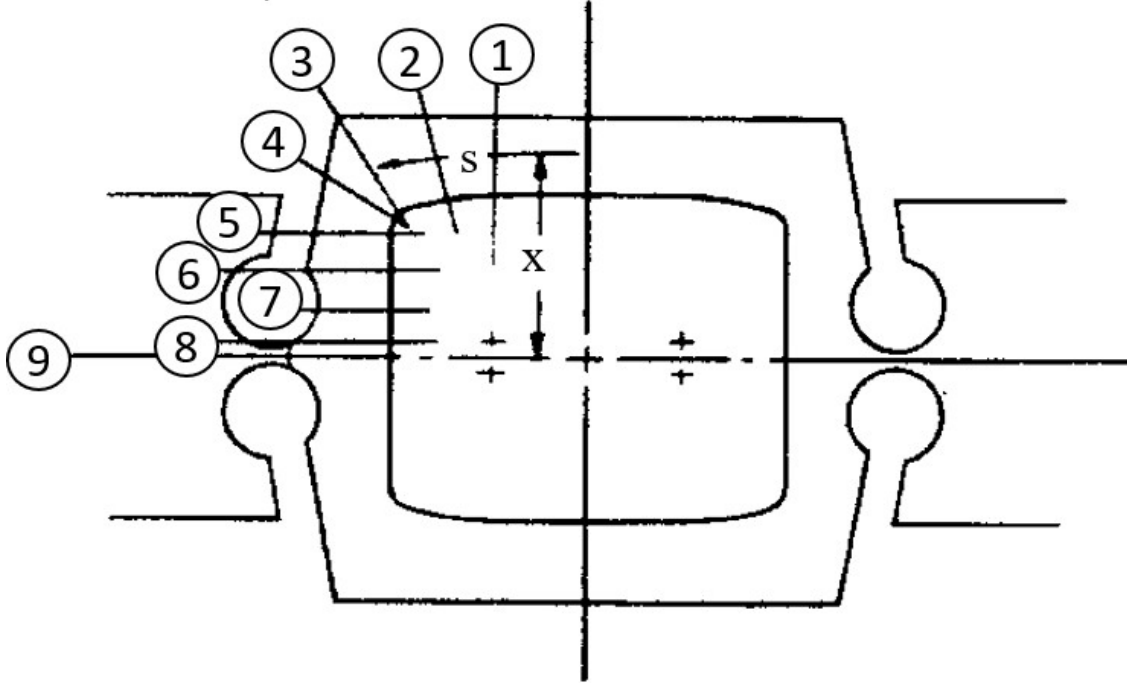


Figure 11: Representation of side force element and chord force element flexures and variables x and s [26]

The offset distance from the magnitude of the redundant moment (x_a) is determined using equation 7:

$$x_a = \frac{\int x/2 \cdot \Delta s / t^3 ds}{\int \Delta s / t^3 ds} \quad (7)$$

where Δs is the change in variable s between intervals (as indexed using circled numbers) as defined in Figure 11. The side force element was subjected to a 750lb compressive load to the top of the element and is fixed at the opposite end, similar to the normal force element, shown in Figure 12. The side force element measures forces in the x -direction.

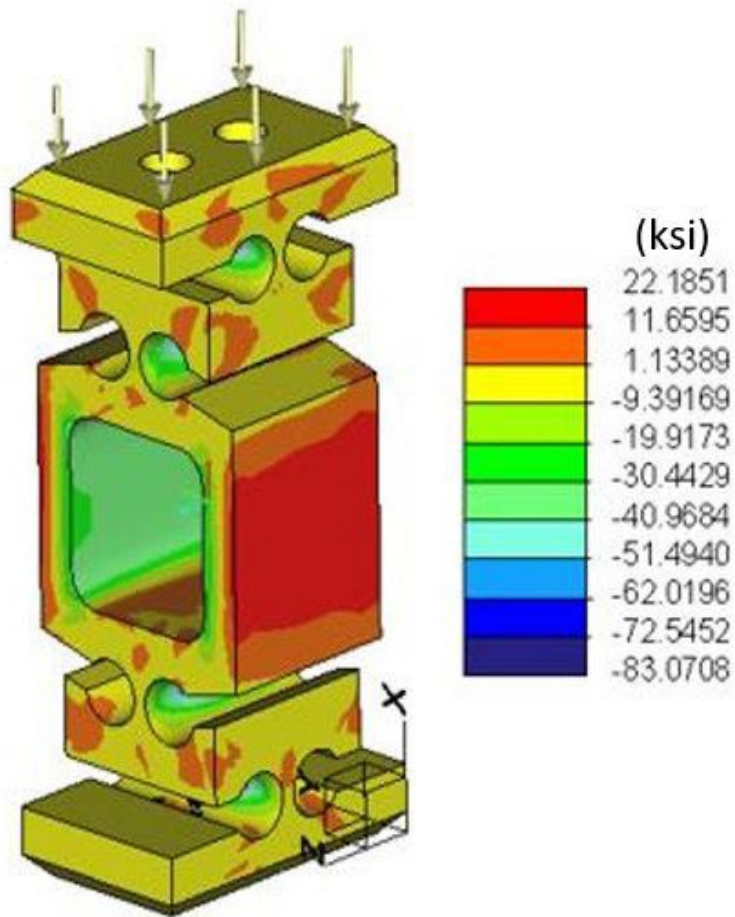


Figure 12: FEA results of side force element undergoing 1500lb rated load – x-directional contour

The chord force element was subjected to a 600lb load applied in the positive z-direction (or axial direction) and is fixed at both the forward and aft sections, shown in Figure 13. The chord force element measures forces in the z-direction.

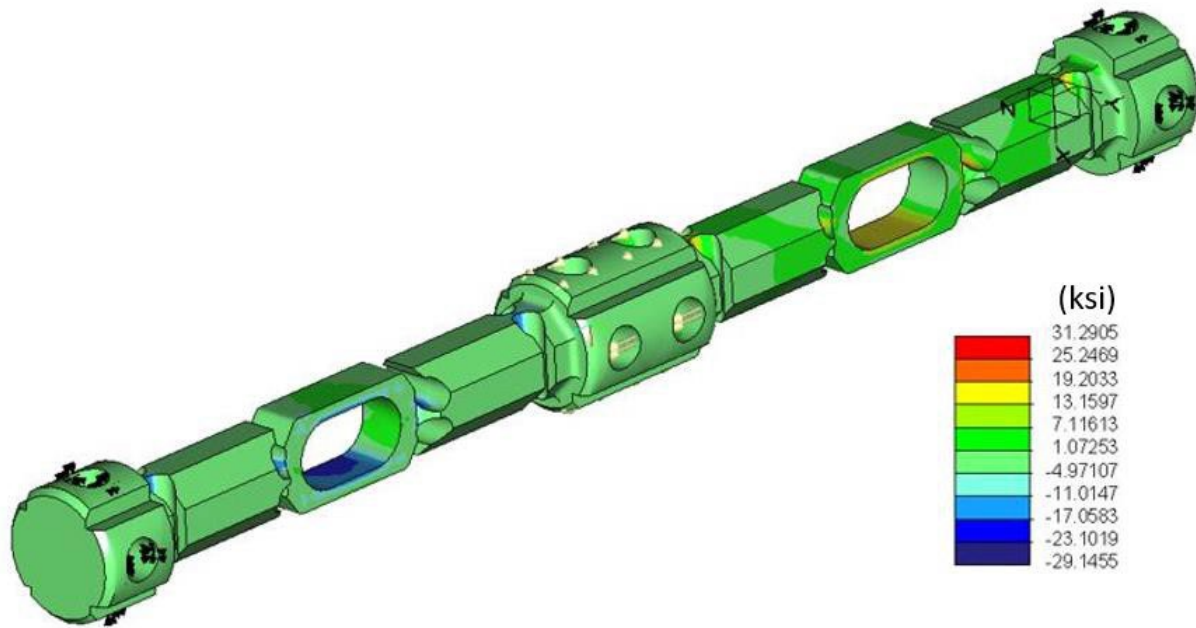


Figure 13: FEA results of chord force element undergoing 600lb rated load – z-directional contour

Finally, the roll cage must be analyzed. The shear stress on the outside of a cylinder is defined as:

$$\tau = \frac{2M}{\pi t D_{avg}^2} \quad (8)$$

where M is the moment applied, t is the thickness of the roll cage walls at the gauge location, and D_{avg} is the average diameter at the gauge location. The values of t and D_{avg} were taken from the section of the roll cage where the gauges are applied, as shown in Figure 6(c). The roll cage experienced a 6000in-lb roll moment around its center and is fixed at the forward and aft ends. Figure 14 shows the results of the FEA.

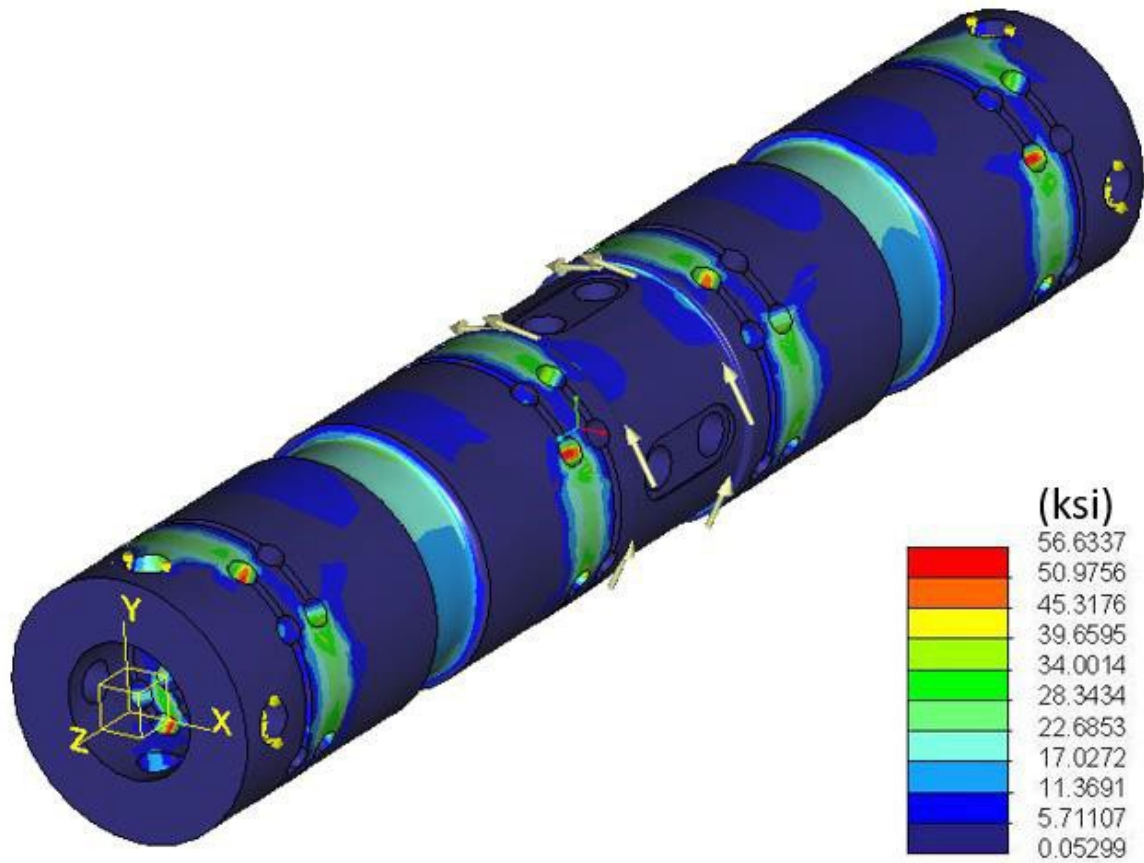


Figure 14: FEA results of roll cage undergoing 6000in-lb rated moment – Shear contour

The assembly was also tested under the same rated loads, and stress values were captured at the same locations and in the same axial directions as the individual components. The results from the theoretical, individual, and assembly testing are found in Table 2. The comparison between the theoretical data and the individual FEA data show very minor error. This indicates that the individual components are near close to the dimensions expected, as they are following the theoretical data that was used in the stress report [26]. When the FEA is conducted using the whole assembly, however, the results were remarkably lower than the theoretical results. Specifically, the normal stress was down by 13.77%, the side stress was down by 27.06%, and

the axial force was down by 26.08%, yet the shear force was about the same as the theoretical and the individual FEA. This is analyzed further in Section 2.2.3.

Table 2: Stress values in force balance components with theoretical calculations, individual FEA, and assembly FEA (ksi)

<i>Part</i>	<i>Theoretical</i>	<i>Individual FEA (error)</i>	<i>Assembly FEA (error)</i>
<i>Normal</i>	30.5	31.9 (4.59%)	26.3 (-13.77%)
<i>Side</i>	35.1	36.6 (4.27%)	25.6 (-27.06%)
<i>Axial</i>	16.2	16.7 (3.08%)	12.1 (-26.08%)
<i>Roll Cage</i>	34.2	33.2 (-2.92%)	32.9 (-3.80%)

2.2.2 Strain gauge reading analysis

This section handles the calibration of the gauge readings on the force balance. Each component contains 4 strain gauges to complete a Wheatstone bridge, a diagram of which is shown in Figure 15.

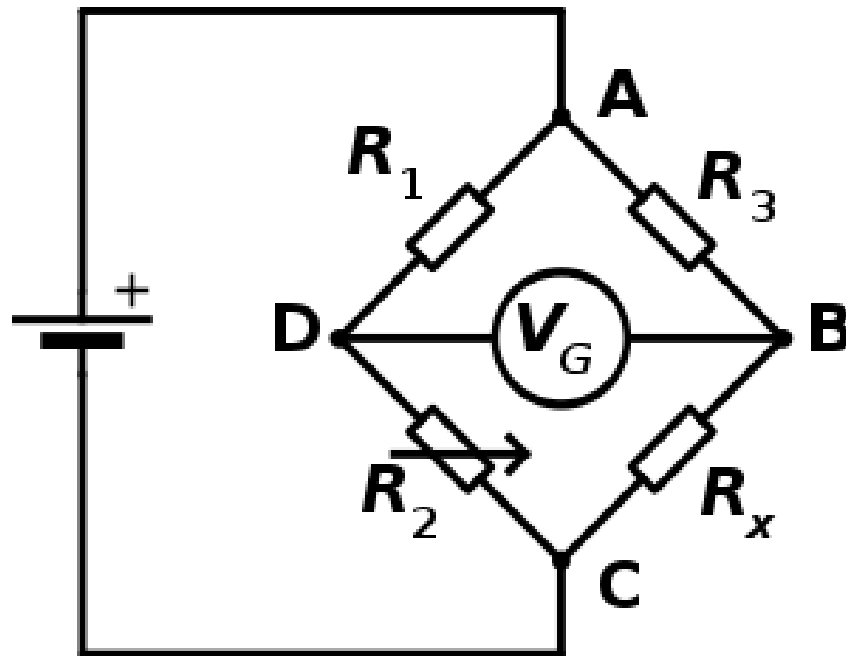


Figure 15: Wheatstone bridge diagram

To find the bridge output, the following equation must be used,

$$V_r = K \frac{(\varepsilon_1 + \varepsilon_2) - (\varepsilon_3 + \varepsilon_4)}{4} \quad (9)$$

where K is the gauge factor ($=2.2 \times 10^6 \mu\Omega/\Omega$) [57], V_r is the bridge reading output in $\mu V/V$, and ε_i are the strain gauge readings where i dictates the location of the strain gauge location. The force balance was tested at the normal, side, axial, and roll rated loads and the strains were measured from the gauge locations as indicated in Figure 6 and Section 2.1.2. Cross-axis coupling was also analyzed during these tests. It was found that all instances of cross-axis coupling were remarkably small, for example, when the balance was tested under a normal force, the normal force element gauges read strains over 1000 times larger than other components. Therefore, any cross-axis coupling should not be a concern for this balance.

The calibration data was taken from a test completed on this balance in 2008 [60]. This report did not test the balance at the rated loads, likely due to the risk of failure at rated loads as was shown in Bennet's force balance [25]. The relationship between force and gauge reading is linear, so converting an expected gauge reading for a rated load requires scaling the ratio of the rated load. For example, the normal force calibration was 1000lb and the rated load is 3000lb. Therefore, the gauge reading must be scaled by 3 to give an expected gauge reading. It is noted that all comparisons to the calibration data will be shown by a percentage difference with the FEA data¹.

The expected gauge readings were converted linearly to match the rated loads, and an FEA was conducted for each rated load as a full assembly. Table 3 displays the scaled calibration

¹ The actual calibration data cannot be displayed due to the data being proprietary.

results compared to the FEA results. The results show that the side force element provides a satisfactory level of gauge reading, but the other components show a large error between the FEA and calibration results. This is tied to the same issue causing the force discrepancy in the assembled force balance in Section 2.2.1. This discrepancy is analyzed further in Section 2.2.3.

Table 3: Calibration vs. FEA gauge reading results

<i>Component</i>	<i>FEA ($\mu V/V$)</i>	<i>Error from Calibration [60]</i>
<i>Normal</i>	1925	-31.7%
<i>Side</i>	2877	-8.2%
<i>Chord</i>	526	-58.6%
<i>Roll Cage</i>	1320	-22.3%

2.2.3 Discrepancy analysis on stress and strain gauge reading

As shown in Sections 2.2.1 and 2.2.2, there are stress discrepancies in the normal, side, and chord force element in Table 2 and the gauge reading discrepancies in the normal and chord force element. This section conducted another FEA test by monitoring the stress value in the normal force element gauge section while the element is in an assembly and comparing it to the stress experienced by the part individually. The side force element, chord force element, and the roll cage were added separately with the normal force element in the assembly. It was found that by adding the side and chord force elements, the stress value in the normal force element decreased by 2.1% each, but by adding the roll cage, the stress value in the normal force element decreased by 19.9%. This notable drop in stress in the normal force element when the roll cage was added to the assembly shows the issue is within the roll cage.

It is concluded that the roll cage is too stiff, causing a reduction in stress values when all components are in an assembly, therefore causing a reduction in gauge readings. Therefore, some design change to reduce the stiffness must occur to alleviate these discrepancies. The hinge thickness is the most sensitive dimension to change the stiffness of the roll cage, and the

parameter study is additionally conducted to reduce stiffness. To find an ideal hinge thickness, the hinge thickness was tested on a 20% reduction interval, and the total force balance assembly was tested under rated normal force loads as a representative of the other components. The stress in the normal force element was then recorded, as shown in Table 4.

Table 4: Stress in normal force element with varied roll cage flexure hinge thicknesses

<i>Reduction in thickness</i>	<i>Stress (ksi)</i>
0%	26.3
20%	30.7
40%	31.0
60%	31.3
80%	31.5

The results of this test showed that decreasing the hinge thickness increases the stress value in the normal force element, as expected. By the time the thickness had reached an 80% reduction, the stress in the normal force element was 31.5ksi, which is close to the desired stress value of 31.9ksi, as measured in the individual stress test displayed in Table 2. The hinge thickness location can be seen in Figure 16, and the 80% reduction in the hinge thickness can be shown in Figure 17.

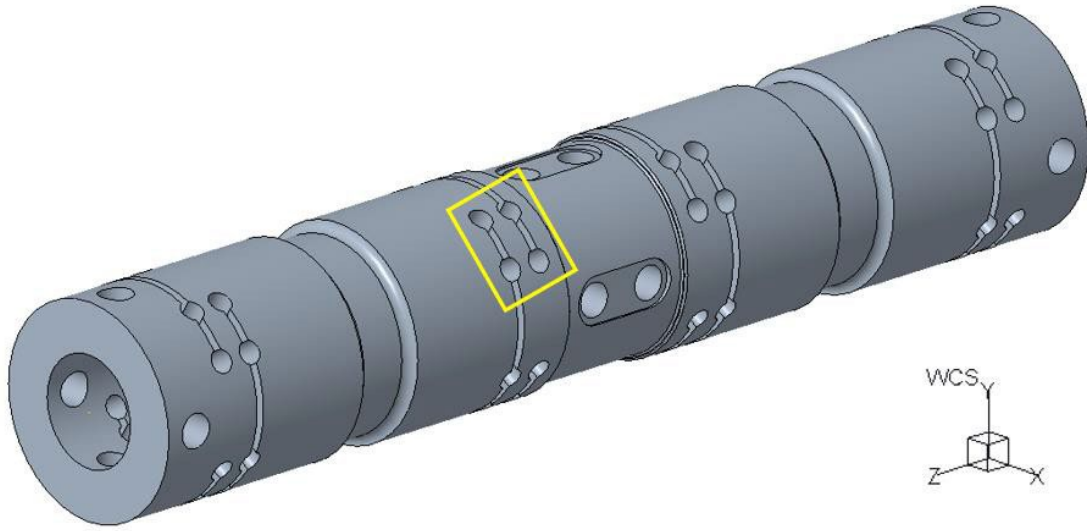


Figure 16: Roll cage flexure location

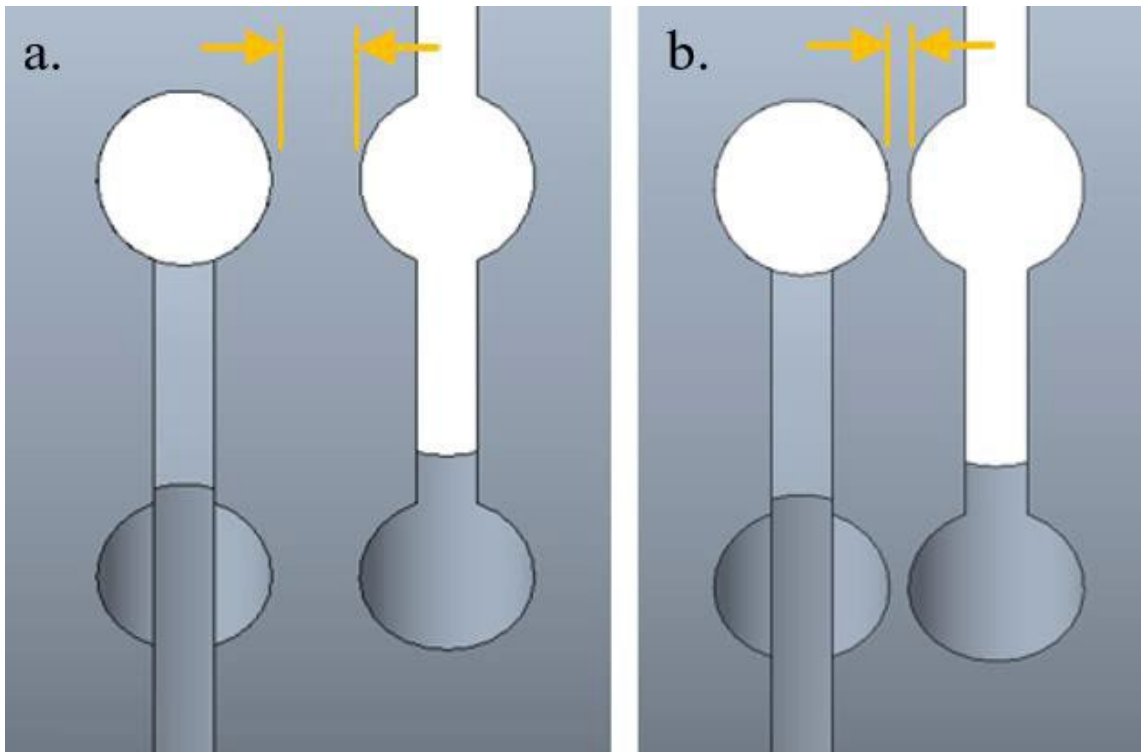


Figure 17: Enhanced view of roll cage flexure. (a) Original roll cage flexure dimensions. (b) 80% reduction in hinge thickness roll cage flexure.

The altered roll cage was placed in an assembly and the same tests in Sections 2.2.1 and 2.2.2 were conducted. The stress values of the balance at rated loads are shown in Table 5.

Table 5: Stress values in force balance components with theoretical calculations, individual FEA, and assembly FEA with updated roll cage (ksi)

<i>Component</i>	<i>Theoretical</i>	<i>Individual FEA (error)</i>	<i>Assembly FEA (error)</i>
<i>Normal</i>	30.5	31.9 (4.59%)	31.5 (3.27%)
<i>Side</i>	35.1	36.6 (4.27%)	31.2 (-11.11%)
<i>Axial</i>	16.2	16.7 (3.08%)	16.4 (1.23%)
<i>Roll Cage</i>	34.2	33.2 (-2.92%)	31.3 (-8.47%)

The reduction in stiffness of the roll cage increased the stress values in the normal, side, and chord force elements when in an assembly. The stress of the roll cage in an assembly decreased at the gauge locations, but there are a few adverse effects caused by decreasing the hinge thickness of the roll cage. Firstly, manufacturing of the piece would be more difficult, for the size of the hinge thickness is small close to the tolerance value. Secondly, the maximum stress the piece experiences increases. Under a 6000in-lb roll moment, similar to the analysis conducted in Section 2.2.1, the roll cage experiences a maximum von Mises stress of 263.5ksi, which is notably higher than the original maximum von Mises stress of 106.1ksi.

The calibration data with the updated roll cage is shown in Table 6.

Table 6: Calibration vs. FEA gauge reading results with updated roll cage

<i>Component</i>	<i>FEA ($\mu V/V$)</i>	<i>Error from Calibration [60]</i>
<i>Normal</i>	2316	-17.8%
<i>Side</i>	3569	13.8%
<i>Chord</i>	777	-38.8%
<i>Roll Cage</i>	1325	-22.0%

As expected, the gauge readings for the normal, side, and chord force elements increased by a large margin. Although the values are not exact to the calibration data, the values are in a more satisfactory position than they were previously in Table 3. The roll cage gauge reading did not change as much as the other components. This is due to the fact that changing the dimensions of

the flexure on the roll cage did not alter the amount of moment being transferred to the gauge section of the roll cage, therefore outputting near close to the same gauge output.

Although decreasing the roll cage flexure hinge thickness reduced the discrepancies shown in the stress and gauge reading calibration data, it generated the structural safety issue. There should be more systematic approach to determine the optimal values of the multiple parameters.

It is more important to keep to known dimensions of the force balance than to attempt to make the force balance model fit the stress and gauge reading data. However, this analysis was important to understand the reduction of force in the assembly, and this information can be utilized in further designs. This analysis also displayed that changing the hinge thickness of the roll cage can alter the stiffness of the roll cage, in turn effecting the amount of maximum stress it experiences. This knowledge will prove useful in selecting a variable for optimization. The study will proceed with the original hinge thickness in the roll cage.

2.3 Maximum stress analysis of force balance

To analyze what maximum stresses the balance underwent at its current rated loads, the balance model underwent each weighted load in FEA study, as defined in Table 1. The balance can only undergo a full rated normal force or a full rated pitch moment. The same trade-off is found with the side force and the yaw moment. Therefore, there are two scenarios of combined loads described as described in the last two rows of Table 7: normal/side/axial/roll and axial/roll/pitch/yaw. The assembly was put under each stress, and the maximum von Mises stress and the location at which the stress occurred were recorded. The findings are shown in Table 7.

Table 7: Maximum stress analysis of force balance

<i>Force(s)</i>	<i>Max von Mises Stress (ksi)</i>	<i>Location</i>
<i>3000lb Normal</i>	127.3	Normal force member hinge
<i>1500lb Side</i>	56.4	Normal force member hinge
<i>600lb Axial</i>	29.2	Chord force member hinge
<i>6000in-lb Roll Moment</i>	105.4	Roll cage flexure
<i>22500in-lb Pitch Moment</i>	131.1	Normal force member hinge
<i>9750in-lb Yaw Moment</i>	90.7	Normal force member hinge
<i>Normal/Side/Axial/Roll</i>	215.8	Roll cage flexure
<i>Axial/Roll/Pitch/Yaw</i>	158.4	Normal force member hinge

Because no stress value exceeds the ultimate strength of 235ksi of Carpenter 455 stainless steel [26], it shows that this model will not fail under the rated loads.

Two of the highest stress scenarios occurred in the normal force member hinge. These scenarios were: (i) the rated pitch moment scenario (131.1ksi), and (ii) the combined axial/roll/pitch/yaw scenario (158.4ksi). The pitch moment case has 2/3 of the desired ultimate strength, and the second load is only 2ksi above that 156.6ksi value, showing that the balance can well withstand these loads. Figure 18 displays an image of the normal force element within the assembly during the combined load to show the maximum von Mises stress.

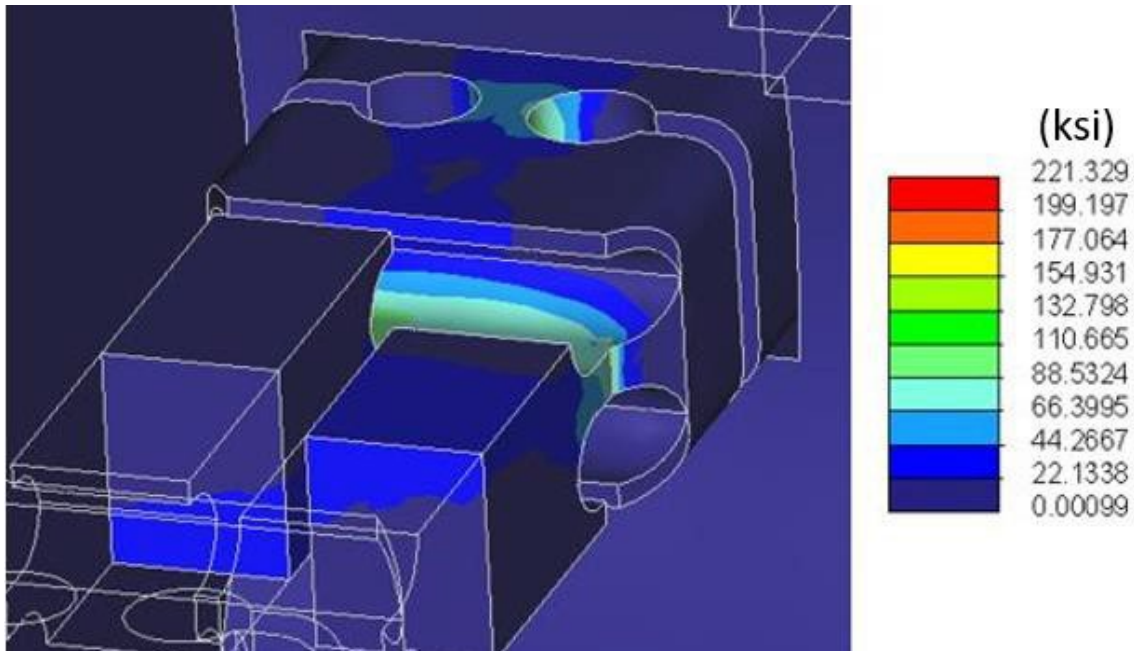


Figure 18: FEA of normal force element in assembly with axial/roll/pitch/yaw combined load – von Mises contour

The other stress concentration occurred within the roll cage flexure during (iii) normal/side/axial/roll scenario (215.8ksi). This maximum stress occurs within the flexure of the roll cage (Figures 19 and Figure 20). This stress is close to the ultimate strength and does not fit the desired 2/3 value of the ultimate strength and will have to be watched as design changes are made. In the design optimization process, it is important to determine design variables while these stress values do not exceed the ultimate strength.

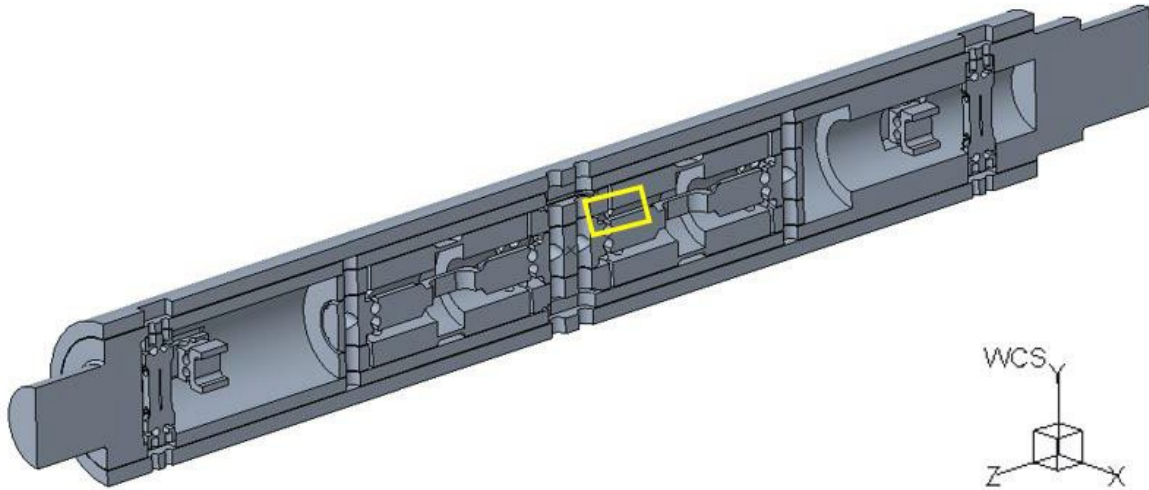


Figure 19: Cross-sectional view of force balance with location of maximum stress under combined rated load

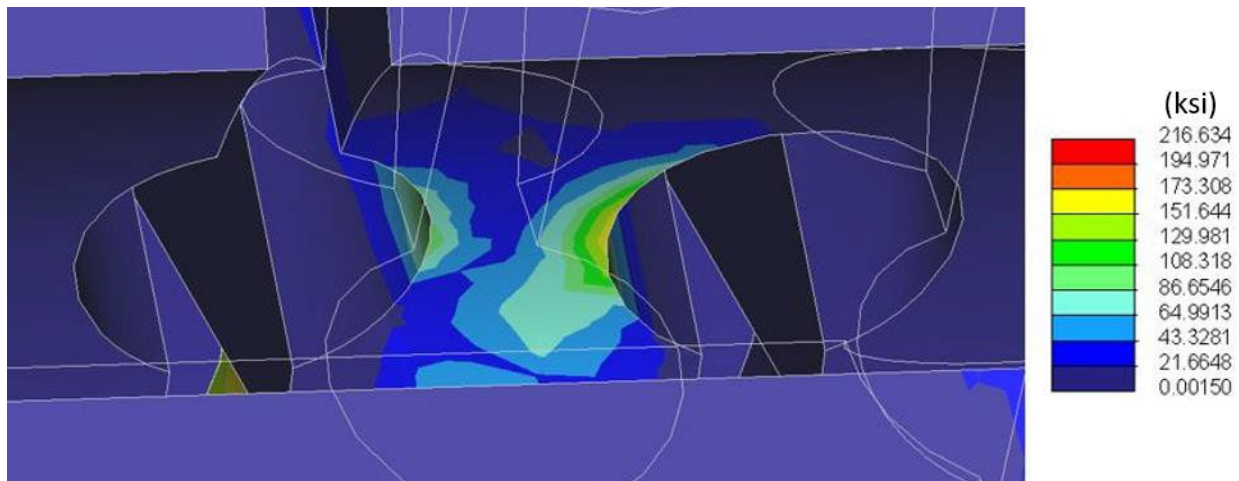


Figure 20: FEA of roll cage flexure in assembly with normal/side/axial/roll combined load – von Mises contour

2.4 Balance response by increased roll moment

In order to get a baseline of how the balance reacts at that rated moment, an FEA must be conducted. Subjected to a 20,000in-lb roll moment only, the original FEA balance model has the maximum von Mises stress of 371.5ksi in the roll cage flexure. This is above the ultimate strength of the material and means failure of the current design. Figure 21 displays location of the maximum stress on the force balance and Figure 22 displays an enlarged view of the stress on the roll cage flexure.

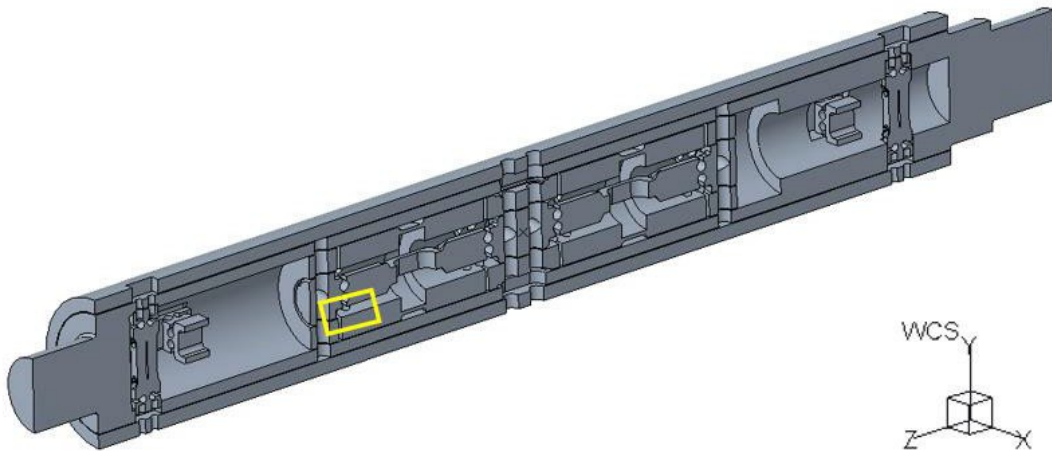


Figure 21: Cross-sectional view of force balance with location of maximum stress

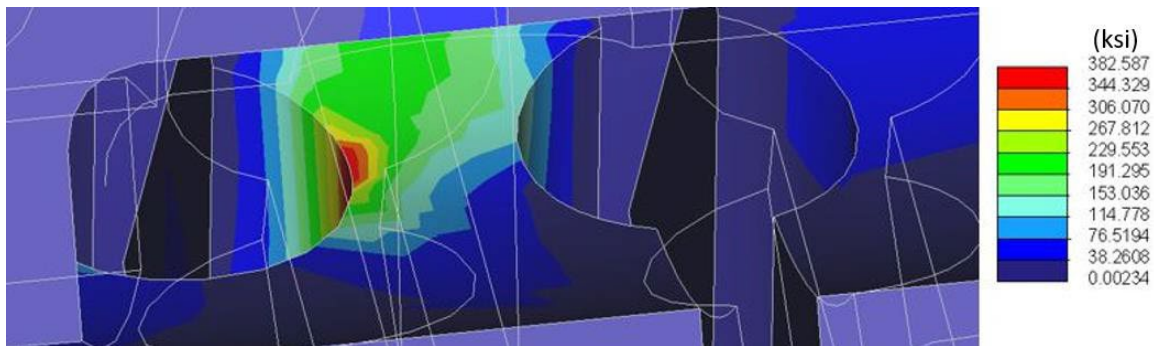


Figure 22: Roll cage flexure under 20,000in-lb moment – von Mises contour

This maximum stress location is similar to that of the rated combined load of the normal/side/axial/roll rated loads, where the maximum stress occurs in the roll cage flexure. The next highest stress concentration in the model is located around the fastener of the roll cage, however this stress was only 153.4ksi, which lies beneath the desired stress level. Therefore, the focus of design change will revolve around the roll cage flexure, for by altering the design of the roll cage flexure, the piece can become stiffer. This stiffness will help reduce the maximum stress experienced within the roll cage by distributing it throughout the balance more evenly.

The gauge reading was also taken from the roll cage at this higher rated load. The reading was found to be 4208 μ V/V, which is remarkably higher than the desired 1700 μ V/V gauge reading.

This target value ($1700\mu\text{V/V}$) is known as the best gauge reading in the force balance considered in this thesis [57]. Therefore, the optimization process will also include a strain component to correct this high gauge reading down to a desired level.

3. Design optimization of balance

This section explains the overall design optimization strategy of the balance to increase the allowed rated roll moment of the force balance from 6000in-lb to 20,000in-lb. For this purpose, a new objective function is proposed that considers stress and strain responses simultaneously. This process involves two steps of response surface method followed by a final, focused regression. In order to get a response by changed design variables, the verified FEA model in Section 2 is used.

3.1 Variables

The balance must remain the same length and total diameter, due to the size of the testing rig that the balance will be placed into. Therefore, making the roll cage thicker to decrease the stress concentration or changing the outer profile of the device is improbable. Variables would have to relate to the features within the force balance. Because the maximum stress levels occurred in the flexures of the roll cage, two of the three variables chosen are dimensions of the flexures: the diameter of the hole cutouts in the roll cage flexures (x_1) and the hinge thickness between hole cutouts (x_2). The diameter of the hole cutouts must be between 34.9% and 174.5% of their original dimension ($34.9\% < x_1 < 174.5\%$), whereas the hinge thickness between hole cutouts must be between 46.5% and 820.4% of its original dimension ($46.5\% < x_2 < 820.4\%$). The

variables can be seen in Figure 23, the diameter being the blue dimension and the hinge thickness being the yellow dimension.

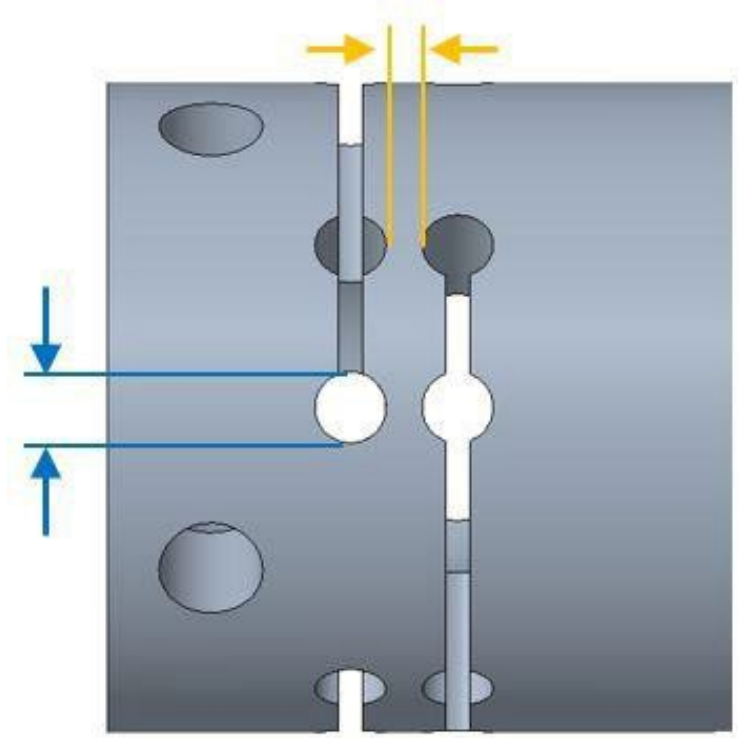


Figure 23: Roll cage flexure variables, hole cutout diameter (blue) and hinge thickness (yellow)

The third variable is the thickness of the roll cage gauge location (x_3) to help lower the $4208\mu\text{V/V}$ gauge reading to the desired value of $1700\mu\text{V/V}$. As shown in Figure 7, the area on the roll cage where the gauges are placed has a larger inner diameter and a smaller outer diameter than the rest of the roll cage, creating a thinner cylinder. The inner diameter of the gauge section will be the only dimension changing, while the outer diameter stays constant to allow space for the gauges when the roll cage is inserted into the inner rod. The roll cage gauge location thickness dimensions must stay between 8.33% and 433.3% of its original dimensions ($8.33\% < x_3 < 433.3\%$). Figure 24 displays a focused image on the dimension to be modified for this process.

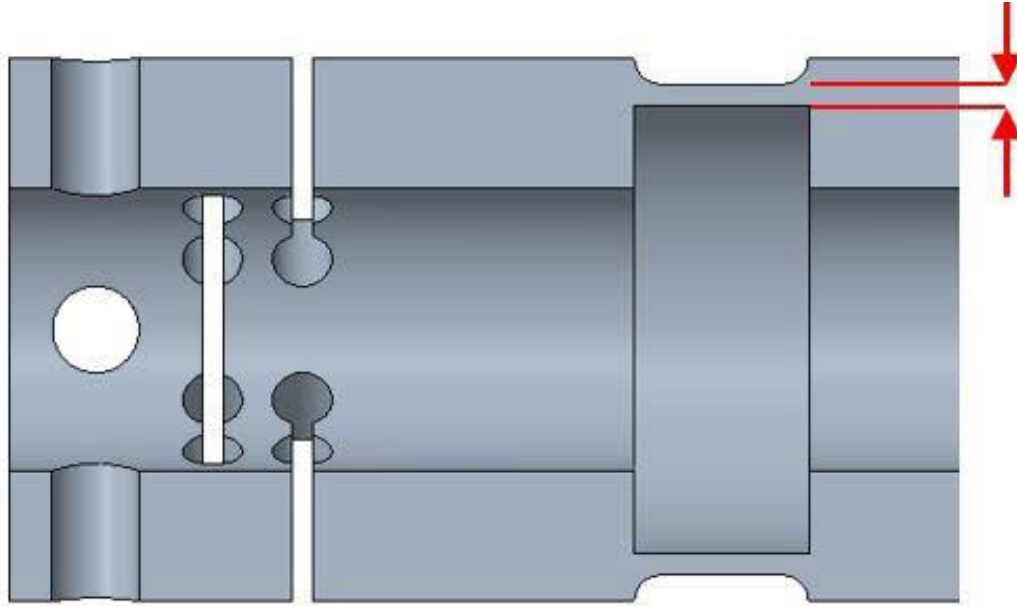


Figure 24: Roll cage gauge location thickness variable, referenced at the outer surface

3.2 Sampling for Response Surface Method

For this study, three sampling techniques for RSM were chosen and compared: Central Composite Circumscribed (CCC), Central Composite Face-centered (CCF), and the Box-Behnken (BB) method [59]. The CCC and CCF methods fall under the central composite design (CCD) sampling methods. Figures 25-27 display a sample layout for the CCC, CCF, and (BB) methods, respectfully, when there are three design variables. For each of these methods, a center point is selected, and subsequent points are found using different step sizes away from the center point.

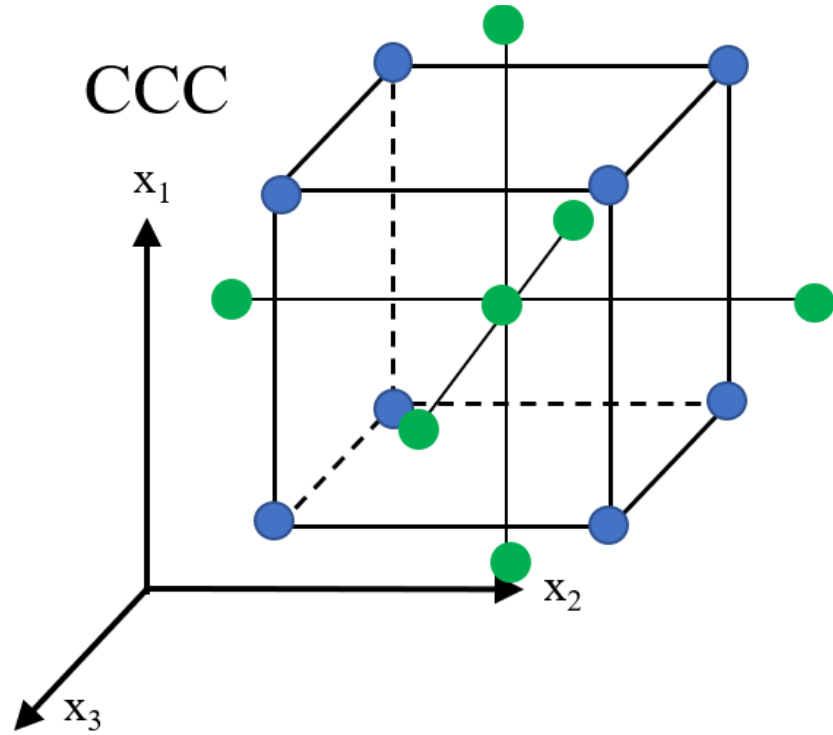


Figure 25: A 3-dimensional representation of a CCC sampling

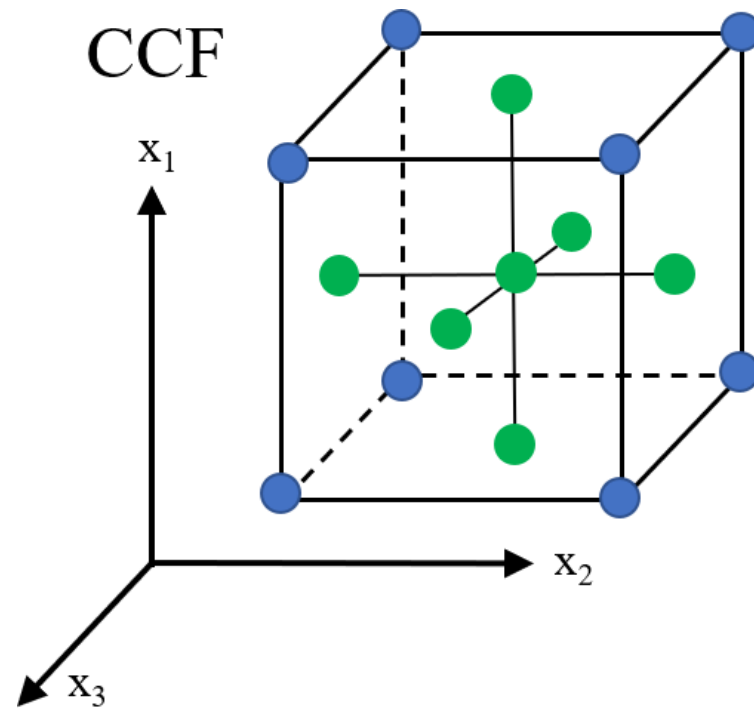


Figure 26: A 3-dimensional representation of a CCF sampling

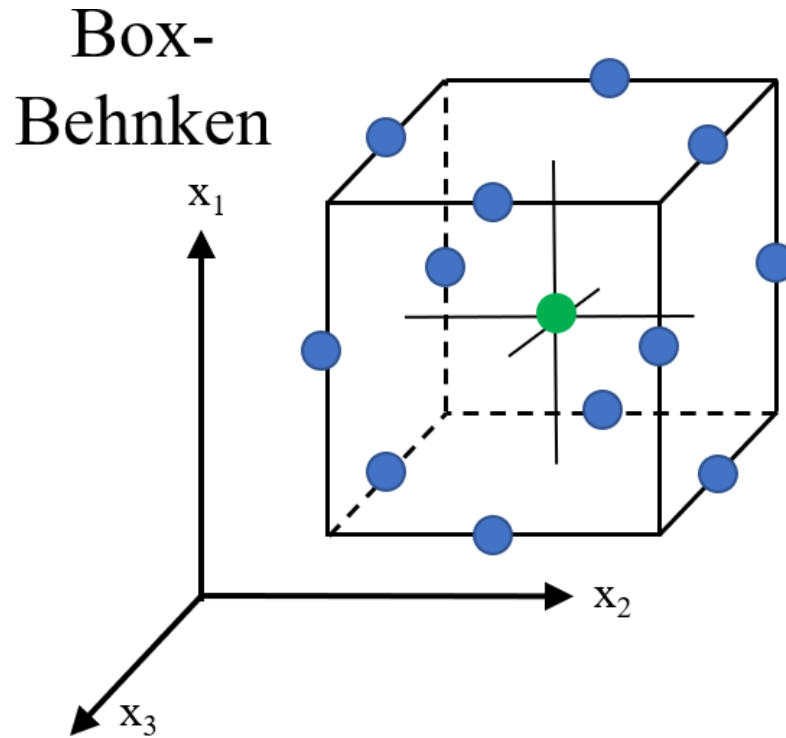


Figure 27: A 3-dimensional representation of a BB sampling

Figures 25 and 26 contain blue and green sample points on their plots. The green points represent the main impact sample points, which consist of points that only vary a single variable at a time, while keeping the other variables constant. The blue points represent the combined sample points, which involve altering more than one variable. The single green point shown in Figure 27 represents the center point.

Table 8 displays an example of these sampling techniques when three variables are considered.

Table 8: CCC, CCF, and BB sampling example

CCC			CCF			BB		
x_1	x_2	x_3	x_1	x_2	x_3	x_1	x_2	x_3
0	0	0	0	0	0	0	0	0
1	0	0	1	0	0	1	1	0
-1	0	0	-1	0	0	1	-1	0
0	1	0	0	1	0	1	0	1
0	-1	0	0	-1	0	1	0	-1
0	0	1	0	0	1	-1	1	0
0	0	-1	0	0	-1	-1	-1	0
1.68	1.68	1.68	1	1	1	-1	0	1
1.68	1.68	-1.68	1	1	-1	-1	0	-1
1.68	-1.68	1.68	1	-1	1	0	1	1
1.68	-1.68	-1.68	1	-1	-1	0	1	-1
-1.68	1.68	1.68	-1	1	1	0	-1	1
-1.68	1.68	-1.68	-1	1	-1	0	-1	-1
-1.68	-1.68	1.68	-1	-1	1			
-1.68	-1.68	-1.68	-1	-1	-1			

3.3 Response Surface Modeling

The RSM process used in this thesis is shown through Figure 28. The process begins by sampling through CCC, CCF, and BB, as described in Section 3.2. That sampled data is then used to find the coefficient values for the multi-objective function that will be explained later in this section. The optimized best points are found using the quadratic multi-objective function using different weight combinations, and the best point is selected. The best point's expected values are then compared with FEA results. If the expected values are close to the actual values, then the accurate best point for that sampling method has been found. If not, more sampling will have to be conducted to make a more accurate model. This process is explained in further detail within this section.

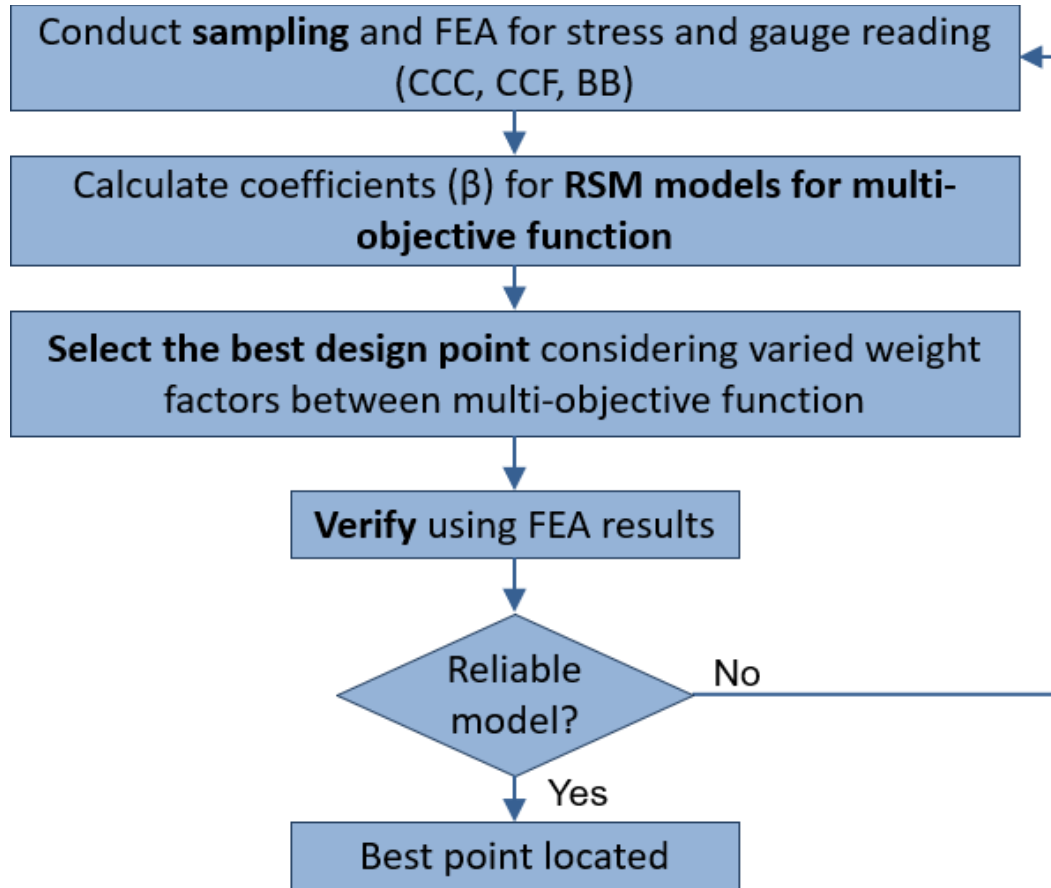


Figure 28: Design process flow chart

For this stepwise response surface method, two trials were conducted. Trial 1 was conducted using the original dimensions as the center point for sampling. In Trial 2, the center point was based around the results of Trial 1, as well as other subsequent testing, which will be further explained in 3.4.2.

RSM can fit empirical models to a set of experimental data [61]. The model that was used in this study was a second order polynomial that allows for interactions between the experimental variables:

$$y = \beta_0 + \sum_{i=1}^N \beta_i x_i + \sum_{i=1}^N \sum_{j=1}^N \beta_{ij} x_i x_j \quad (10)$$

where x_i represents the i th variable, N is the total number of design variables, β_0 is the constant term, β_i is the coefficient related to the linear terms of x_i , and β_{ij} is the coefficient in the second order relating coefficients x_i and x_j . Note that if i and j are the same value, the coefficient becomes β_{ii} and relates to the quadratic term x_i^2 . For this study, three variables are chosen. Coefficients β_{11} , β_{22} , and β_{33} will be represented by coefficients $\beta_4 \sim \beta_6$. Coefficients β_{12} , β_{13} , and β_{23} will be represented by coefficients $\beta_7 \sim \beta_9$. Because two models are created, one for stress and one for gauge reading, two sets of coefficients are created. Coefficients $\beta_0 \sim \beta_9$ will represent the stress model, and coefficients $\beta_{10} \sim \beta_{19}$ will represent the gauge reading model.

In order to achieve a more accurate empirical model for the study, weighted regression was used to solve for the β coefficient values [61]. The equation for such is as follows:

$$\boldsymbol{\beta} = [\mathbf{x}^T \mathbf{W}(\mathbf{x}) \mathbf{x}]^{-1} \mathbf{x}^T \mathbf{W}(\mathbf{x}) \mathbf{y} \quad (11)$$

where $\mathbf{W}(\mathbf{x})$ is the diagonal matrix for the weight values. It is found that using this model often provides a closer response to the limit state function than an empirical model that uses equal weights for its coefficients (or \mathbf{W} is the identity matrix).

The weight function is found through [61]

$$F(x_l) = y(x_l) - y_{best} \quad l = 1, 2, \dots, L \quad (12)$$

$$\omega_l = \exp \left(- \frac{F(x_l)}{\sum_{j=1}^L F(x_j)} \right) \quad l = 1, 2, \dots, L \quad (13)$$

where y_{best} is the best observation among the sampling points, $y(x_l)$ is the function value at each sampling point, and L is defined as the number of sampled points. In this study, $L = 15$ for CCC and CCF, and $L = 13$ for BB. When all ω_l values are found, the weight matrix can be written as:

$$W(x) = \begin{bmatrix} \omega_1 & 0 & \dots & 0 \\ 0 & \omega_2 & \dots & 0 \\ \dots & \dots & \dots & \dots \\ 0 & 0 & \dots & \omega_L \end{bmatrix} \quad (14)$$

Because both the stress and the gauge reading must be optimized, an empirical model will be generated for both outputs. Once both equations are found, a normalized equation will be created from the two models to minimize:

$$f(x) = \frac{\sigma(x)}{\sigma_0} + \frac{|\varepsilon(x) - 1700|}{\varepsilon_0} \quad (15)$$

where σ_0 is the stress measured at the center point of sampling and ε_0 is the gauge reading measured at the center point of sampling. By finding the minimum of this equation, it is attempting to find the values of the variables that lead to a minimized value of stress and a value of the gauge reading close to the desired 1700 μ V/V value.

For multi-objective optimization perspective, a weighted sum of the objective functions is a usual approach. The function in equation 13 was weighted between stress and gauge reading, as seen in equation 16, and expanded in equation 17:

$$f(x) = w_1 \frac{\sigma(x)}{\sigma_0} + w_2 \frac{|\varepsilon(x) - 1700|}{\varepsilon_0} \quad (16)$$

$$\begin{aligned} f(x) = & w_1(\beta_0 + \beta_1 x_1 + \beta_2 x_2 + \beta_3 x_3 + \beta_4 x_1^2 + \beta_5 x_2^2 + \beta_6 x_3^2 + \beta_7 x_1 x_2 + \beta_8 x_1 x_3 \\ & + \beta_9 x_2 x_3)/\sigma_0 \\ & + w_2(\beta_{10} + \beta_{11} x_1 + \beta_{12} x_2 + \beta_{13} x_3 + \beta_{14} x_1^2 + \beta_{15} x_2^2 + \beta_{16} x_3^2 + \beta_{17} x_1 x_2 \\ & + \beta_{18} x_1 x_3 + \beta_{19} x_2 x_3)/\varepsilon_0 \end{aligned} \quad (17)$$

where weight values w_1 and w_2 must abide by the following statement:

$$w_1 + w_2 = 1 \quad (18)$$

For this study, 11 combinations of w_1 and w_2 were selected, changing by increments of 0.1.

The iterations used in this study of w_1 and w_2 are shown in Table 9.

Table 9: Weight values of w_1 and w_2

w_1	1	0.9	0.8	0.7	0.6	0.5	0.4	0.3	0.2	0.1	0
w_2	0	0.1	0.2	0.3	0.4	0.5	0.6	0.7	0.8	0.9	1

The minimum of $f(x)$ can be found by the first order necessary condition. That is, assuming convexity of $f(x)$, it was differentiated with respect to x_1 , x_2 , and x_3 and set equal to 0, leading to the following equations:

$$\frac{\partial f}{\partial x_1} = w_1 \beta_1 + 2\beta_4 x_1 + \beta_7 x_2 + \beta_8 x_3 / \sigma_0 \quad (19)$$

$$+ w_2(\beta_{11} + 2\beta_{14}x_1 + \beta_{17}x_2 + \beta_{18}x_3)/\varepsilon_0 = 0$$

$$\frac{\partial f}{\partial x_2} = w_1 \beta_2 + 2\beta_5 x_2 + \beta_7 x_1 + \beta_9 x_3 / \sigma_0 \quad (20)$$

$$+ w_2(\beta_{12} + 2\beta_{15}x_2 + \beta_{17}x_1 + \beta_{19}x_3)/\varepsilon_0 = 0$$

$$\frac{\partial f}{\partial x_3} = w_1 \beta_3 + 2\beta_6 x_3 + \beta_8 x_1 + \beta_9 x_2 / \sigma_0 \quad (21)$$

$$+ w_2(\beta_{13} + 2\beta_{16}x_3 + \beta_{18}x_1 + \beta_{19}x_2)/\varepsilon_0 = 0$$

Coefficients $\beta_0 \sim \beta_9$ belong to the stress equation, whereas coefficients $\beta_{10} \sim \beta_{19}$ belong to the gauge reading equation. The solution to these equations is the optimized point. In each trial, there are 3 sampling techniques used, and for each sampling technique there are 11 differently weighted functions, leading to 11 optimized points for each sampling technique. The closest point to the ideal stress and gauge reading value for each sampling method will be focused and discussed.

3.3.1 Trial 1 – Initial Broad Sampling

The center point for the first trial is focused on the original dimensions of the force balance. Each variable had a different step size: $x_1 = 37.5\%$, $x_2 = 50.0\%$, and $x_3 = 50.0\%$, respectively. x_1 variable was set to a 37.5% step size rather than 50% because it was the largest step size possible before x_1 samples reached below the lower bound. Samples were taken from the finite element model after it underwent a 20,000in-lb roll moment. Tables 10~12 display the sampling results

from CCC, CCF, and BB. It is important to note that the variables shown in the table are represented by the step sizes from the center point, rather than the actual dimensions.

Table 10: Trial 1 CCC sampling data

x_1	x_2	x_3	Maximum von Mises stress (ksi)	Gauge reading ($\mu\text{V/V}$)
0	0	0	370.7	4208.2
1	0	0	381.1	4250.8
-1	0	0	380.9	4222.4
0	1	0	312.5	4475.2
0	-1	0	501.8	4264.9
0	0	1	351.8	2995.0
0	0	-1	371.6	7901.1
1.68	1.68	1.68	304.3	2626.3
1.68	1.68	-1.68	912.5	35077.0
1.68	-1.68	1.68	1089.3	2571.5
1.68	-1.68	-1.68	1094.1	24312.7
-1.68	1.68	1.68	317.4	2570.9
-1.68	1.68	-1.68	738.6	24135.5
-1.68	-1.68	1.68	1203.6	2616.8
-1.68	-1.68	-1.68	1122.6	23944.0

Table 11: Trial 1 CCF sampling data

x_1	x_2	x_3	Maximum von Mises stress (ksi)	Gauge reading ($\mu\text{V/V}$)
0	0	0	370.7	4208.2
1	0	0	381.1	4250.8
-1	0	0	380.9	4222.4
0	1	0	312.5	4475.2
0	-1	0	501.8	4264.9
0	0	1	351.8	2995.0
0	0	-1	371.6	7901.1
1	1	1	324.2	3060.0
1	1	-1	340.1	7966.1
1	-1	1	604.1	3058.8
1	-1	-1	528.8	8047.2
-1	1	1	339.9	3028.9
-1	1	-1	333.5	8104.6
-1	-1	1	536.7	3109.3
-1	-1	-1	545.4	8032.2

Table 12: Trial 1 BB sampling data

x_1	x_2	x_3	Maximum von Mises stress (ksi)	Gauge reading ($\mu\text{V/V}$)
0	0	0	370.7	4208.2
1	1	0	317.7	4340.6
1	-1	0	512.3	4225.3
1	0	1	414.4	3013.2
1	0	-1	420.2	7956.9
-1	1	0	337.9	4469.8
-1	-1	0	571.5	4262.3
-1	0	1	412.8	3012.4
-1	0	-1	392.2	7867.2
0	1	1	306	3059.5
0	1	-1	307.2	7719.9
0	-1	1	483.9	3021.8
0	-1	-1	484.7	7674.4

It is important to note that during CCC sampling in Trial 1, as shown in Table 10, four instances occurred where the gauge reading reached above $20,000\mu\text{V/V}$. These instances occurred when $x_3 = -1.68$ its step size. This occurs because the gauge location thickness (x_3) is extremely thinner close to its lower bound, and large deformations occur at this thin gauge section which the gauge reading is taken from.

The coefficients for both the stress and the gauge coefficient models for CCC, CCF, and BB are obtained using equation 11, as shown in Table 13.

Table 13: Trial 1 model coefficient values

Coefficient	CCC	CCF	BB
β_0	1.50E+03	9.32E+02	9.63E+02
β_1	-4.83E+03	-2.04E+03	-3.34E+03
β_2	-1.02E+04	-6.49E+03	-5.09E+03
β_3	-3.00E+03	-7.01E+02	5.78E+02
β_4	1.40E+04	6.18E+03	9.27E+03
β_5	4.63E+04	2.84E+04	1.34E+04
β_6	4.33E+04	6.93E+03	6.88E+02
β_7	4.81E+03	-2.63E+03	3.08E+03
β_8	-6.38E+03	3.47E+03	-3.44E+03
β_9	-3.82E+04	-7.12E+03	-1.83E+02
β_{10}	2.80E+04	1.27E+04	1.27E+04
β_{11}	-5.48E+04	5.83E+02	5.83E+02
β_{12}	-7.65E+04	-1.01E+04	-1.01E+04
β_{13}	-4.37E+05	-2.43E+05	-2.43E+05
β_{14}	1.99E+05	-2.73E+03	-2.73E+03
β_{15}	5.21E+05	6.59E+04	6.59E+04
β_{16}	2.37E+06	1.34E+06	1.34E+06
β_{17}	1.51E+05	-2.42E+03	-2.42E+03
β_{18}	-2.51E+05	6.48E+03	6.48E+03
β_{19}	-3.64E+05	-8.27E+03	-8.27E+03

With these coefficients and equations 19~21, the corresponding optimized points were found for each combination of the weight². We investigated the projected stress, gauge reading, as well as the distance away the point is from an ideal minimized stress and a gauge reading of 1700 μ V/V. The projected values are found using the regression function with the β coefficients within Table 13. The actual values are found by running an FEA. The distance from the ideal point is measured using the normalized stress and gauge reading data as the following equation:

² The actual values of the variables in each point cannot be shown due to proprietary information with NASA Langley Research Center

$$d = \sqrt{\left(\frac{\sigma}{\sigma_0}\right)^2 + \left(\frac{\varepsilon - 1700}{\varepsilon_0}\right)^2} \quad (22)$$

In the normalized dimension, the ideal point lies at (0,0), for the goal is to minimize the stress and to achieve a gauge reading of 1700. Table 14 shows this investigation for the CCC sampling.

Table 14: Trial 1 CCC optimized points data

w_1	w_2	σ (ksi)	ε ($\mu V/V$)	σ/σ_0	$(\varepsilon-1700)/\varepsilon_0$	Distance from ideal point
1	0	157.7	70.0	0.4255	-0.3873	0.5754
0.9	0.1	159.6	-336.8	0.4304	-0.4840	0.6477
0.8	0.2	164.7	-667.6	0.4443	-0.5626	0.7169
0.7	0.3	173.0	-949.8	0.4666	-0.6297	0.7837
0.6	0.4	184.4	-1190.8	0.4974	-0.6869	0.8481
0.5	0.5	199.0	-1393.8	0.5369	-0.7352	0.9104
0.4	0.6	216.9	-1560.1	0.5852	-0.7747	0.9709
0.3	0.7	238.2	-1690.1	0.6426	-0.8056	1.0305
0.2	0.8	263.0	-1783.8	0.7094	-0.8279	1.0902
0.1	0.9	291.4	-1840.7	0.7861	-0.8414	1.1514
0	1	323.6	-1859.9	0.8730	-0.8459	1.2156

The optimized point with the shortest distance to ideal occurs when $w_1 = 1$, meaning this point was determined solely by optimizing the stress function. At this point, x_1 is 100.4% of its original dimension, x_2 is 171.9% of its original dimension, and x_3 is 187.6% of its original dimension. This point was then tested in the FEA to compare to the expected stress and gauge reading values. The comparison is shown in Table 15.

Table 15: Trial 1 – CCC optimized point output comparison

	Equation	FEA
Stress (ksi)	157.7	309.2
Gauge reading ($\mu V/V$)	70.0	2527.0

The model generated from the CCC sampling in Trial 1 was found to be quite inaccurate and would not make a sufficient representation of the force balance. This inaccuracy is most likely due to the wide variance in CCC sampling. CCC sampling has a wider variance (± 1.68) than

CCF or BB sampling, so CCC sampling's wide variance combined with Trial 1 being a wide initial collection of data most likely led to a highly nonlinear variation of the performance. That varied set of data, when interpreted as a quadratic model, resulted in an inaccurate interpretation of the force balance.

The same process was conducted for CCF sampling. The optimized points data is shown in Table 16.

Table 16: Trial 1 CCF optimized points data

w_1	w_2	σ (ksi)	ϵ ($\mu\text{V}/\text{V}$)	σ/σ_0	$(\epsilon-1700)/\epsilon_0$	Distance from ideal point
1	0	303.1	3453.1	0.8175	0.4166	0.9175
0.9	0.1	303.8	3138.4	0.8196	0.3418	0.8880
0.8	0.2	304.3	3106.2	0.8208	0.3342	0.8862
0.7	0.3	304.7	3091.1	0.8220	0.3306	0.8860
0.6	0.4	305.3	3078.2	0.8237	0.3275	0.8864
0.5	0.5	306.3	3064.5	0.8264	0.3242	0.8877
0.4	0.6	308.1	3048.5	0.8311	0.3204	0.8907
0.3	0.7	311.3	3029.1	0.8398	0.3158	0.8972
0.2	0.8	317.7	3005.5	0.8570	0.3102	0.9115
0.1	0.9	332.1	2978.2	0.8958	0.3037	0.9459
0	1	370.4	2960.9	0.9991	0.2996	1.0430

The spread of expected normalized outputs from the CCF sampling was more consistent than the CCC sampling. The shortest distance for CCF sampling occurred when $w_1 = 0.7$ and $w_2 = 0.3$. The optimized point's variables are: $x_1 = 97.7\%$, $x_2 = 150.2\%$, and $x_3 = 148.5\%$ of its original dimension. Similar to CCC sampling, x_1 roughly stayed close to original, whereas variables x_2 and x_3 increased by around 50% of their original value. This point was then tested in the FEA to compare to the expected stress and gauge reading values. The comparison is shown in Table 17. The model found from CCF sampling was fairly accurate, having a 3.02% stress error and a 4.24% gauge reading error.

Table 17: Trial 1 – CCF optimized point output comparison

	Equation	FEA
Stress (ksi)	304.7	313.9
Gauge reading ($\mu V/V$)	3091.1	2960.0

Finally, in Trial 1, the same process was done for the BB sampling. The optimized points data is shown in Table 18.

Table 18: Trial 1 BB optimized points data

w_1	w_2	σ (ksi)	ϵ ($\mu V/V$)	σ/σ_0	$(\epsilon-1700)/\epsilon_0$	Distance from ideal point
1	0	269.9	25012.2	0.7281	5.5397	5.5874
0.9	0.1	275.7	3419.4	0.7437	0.4086	0.8486
0.8	0.2	276.6	3358.8	0.7462	0.3942	0.8440
0.7	0.3	278.2	3305.8	0.7505	0.3816	0.8419
0.6	0.4	280.8	3251.2	0.7575	0.3686	0.8424
0.5	0.5	284.9	3194.5	0.7686	0.3551	0.8467
0.4	0.6	291.2	3136.2	0.7857	0.3413	0.8566
0.3	0.7	300.8	3078.2	0.8115	0.3275	0.8751
0.2	0.8	315.4	3023.8	0.8508	0.3146	0.9071
0.1	0.9	337.7	2980.1	0.9109	0.3042	0.9603
0	1	372.8	2960.9	1.0058	0.2996	1.0495

Similar to the testing in CCF, the results from BB sampling proved more consistent than CCC sampling, as most of the distances to the ideal point remained within a small range (0.084~1.05). The best optimized point, similar to CCF sampling, occurred when $w_1 = 0.7$ and $w_2 = 0.3$. The optimized point's variables are: $x_1 = 99.4\%$, $x_2 = 183.6\%$, and $x_3 = 150.5\%$ of its original dimension. This point was tested in the FEA to compare the stress and gauge reading values to the predicted model values as shown in Table 19.

Table 19: Trial 1 – BB optimized point output comparison

	Equation	FEA
Stress (ksi)	278.2	289.4
Gauge reading ($\mu V/V$)	3305.8	3018.1

The model found from BB sampling was also accurate, having a 4.02% stress error and an 8.70% gauge reading error. The BB optimized point resulted in the lowest FEA stress, however, also resulted in the highest FEA gauge reading of the three sampling methods.

A plot of the normalized stress and gauge reading for CCC, CCF, and BB sampling for Trial 1 is summarized in Figure 29. CCF and BB sampling show results that are less varied and more accurate than CCC.

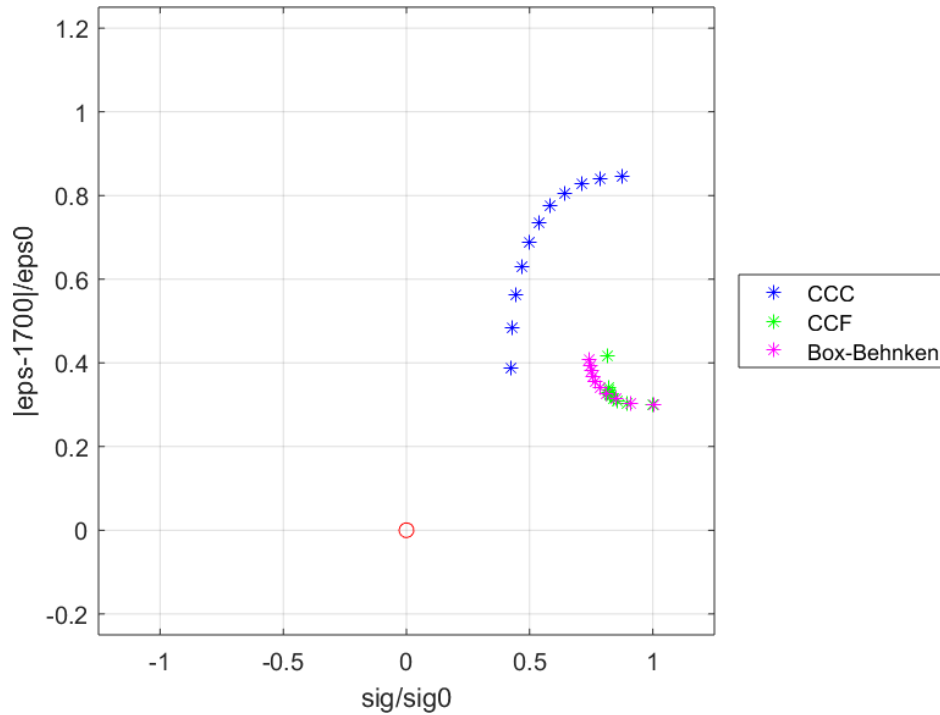


Figure 29: Trial 1 normalized stress and gauge reading plot

Based on the design study in Trial 1, it is required to update the central point and conduct a new design study. All three sampling methods resulted in optimized points where the x_1 value remained close to its original value, but the x_2 and x_3 values increased. Because of this, x_1 will remain the same as the center point for Trial 2. However, the new central point for x_2 and x_3 need to be carefully chosen. Out of Trial 1, it was impossible to have satisfactory level of gauge

reading (around $3000\mu\text{V/V}$, target = $1700\mu\text{V/V}$) as well as the maximum stress values (around 300ksi, target = 156.6ksi). This indicates that x_2 and x_3 need to be studied in a wider range of variation than considered in Trial 1.

To select a new center of x_2 (hinge thickness between hole cutouts), its eight separate values with a larger increment were selected as shown in Table 20 with x_1 and x_3 remaining the constant original dimension. The maximum stress results from this test are found in the same table as well. This test showed that an x_2 value 465% and 581% of the original dimension resulted in the lowest maximum stress values. Choice of the new x_2 center is assumed to be more reliably closer to the optimal value in Trial 1, it was selected to be 465% of the original dimension.

Table 20: Maximum stress values at varying x_2 dimensions

Percentage of original dimension	Maximum stress (ksi)
116%	345.3
233%	268.6
349%	240.4
465%	228.0
581%	228.6
698%	229.1
814%	235.4

Variable x_3 (roll cage gauge location thickness) heavily impacts the gauge reading. That is, by the increased rated roll moment from 6000in-lb to 20,000in-lb, x_3 value should be found to keep the gauge reading close to the ideal $1700\mu\text{V/V}$ value. The change of the gauge reading through Trial 1 (from $4208.2\mu\text{V/V}$ to $3000\mu\text{V/V}$, when the thickness variable changed from 100% to 150%) is assumed to be linear, and a new x_3 value found using extrapolation to be 333.3%.

3.3.2 Trial 2 – Focused Sampling

As described in Section 3.3.1, the center values for Trial 2 are as follows: x_1 = 100% of original dimension, x_2 = 465% of original dimension, and x_3 = 333.3% of original dimension. Similar to

Trial 1, each variable had a different step size: $x_1 = 20\%$, $x_2 = 20\%$, and $x_3 = 10\%$, respectively.

The step sizes for Trial 2 are smaller than those in Trial 1 because the FE analysis for this center is found to be closer to the minimum value of stress and the ideal value of the gauge reading (233.1ksi and 1747.7 μ V/V, respectively), and it enables a more accurate quadratic model within the sample size.

Similar to Trial 1, samples were taken from the finite element model using 20,000in-lb roll moment. Tables 21-23 display the sampling results from CCC, CCF, and BB

Table 21: Trial 2 CCC sampling data

x_1	x_2	x_3	Maximum von Mises stress (ksi)	Gauge reading (μ V/V)
0	0	0	233.1	1747.7
1	0	0	234.4	1807.7
-1	0	0	242.5	1738.1
0	1	0	232.9	1742.7
0	-1	0	274.7	1804.4
0	0	1	239.3	1709.1
0	0	-1	229.9	1873.1
1.68	1.68	1.68	250.1	1762.8
1.68	1.68	-1.68	249.7	2047.3
1.68	-1.68	1.68	253.6	1710.5
1.68	-1.68	-1.68	258.7	1981.3
-1.68	1.68	1.68	243.6	1631.8
-1.68	1.68	-1.68	258	1969.7
-1.68	-1.68	1.68	279.6	1542.7
-1.68	-1.68	-1.68	266.5	1966.3

Table 22: Trial 2 CCF sampling data

x_1	x_2	x_3	Maximum von Mises stress (ksi)	Gauge reading ($\mu\text{V/V}$)
0	0	0	233.1	1747.7
1	0	0	234.4	1807.7
-1	0	0	242.5	1738.1
0	1	0	232.9	1742.7
0	-1	0	274.7	1804.4
0	0	1	239.3	1709.1
0	0	-1	229.9	1873.1
1	1	1	233.3	1709.6
1	1	-1	234.8	1882.0
1	-1	1	245.3	1664.6
1	-1	-1	249.1	1852.0
-1	1	1	235.6	1644.8
-1	1	-1	237.7	1887.2
-1	-1	1	247.5	1685.5
-1	-1	-1	251.1	1870.9

Table 23: Trial 2 BB sampling data

x_1	x_2	x_3	Maximum von Mises stress (ksi)	Gauge reading ($\mu\text{V/V}$)
0	0	0	233.1	1747.7
1	1	0	233	1819.6
1	-1	0	252.9	1801.6
1	0	1	235.1	1721.7
1	0	-1	237.4	1880.0
-1	1	0	241.3	1739.5
-1	-1	0	241.7	1738.3
-1	0	1	251.8	1655.1
-1	0	-1	240.1	1846.7
0	1	1	226.9	1696.9
0	1	-1	233.6	1868.8
0	-1	1	234.3	1678.0
0	-1	-1	240.6	1852.5

The coefficients for both the stress and the gauge coefficient models for CCC, CCF, and BB are as follows in Table 24.

Table 24: Trial 2 model coefficient values

Coefficient	CCC	CCF	BB
β_0	4.78E+01	-6.42E+01	1.77E+02
β_1	9.95E+01	6.05E+02	-7.48E+02
β_2	-1.67E+03	-1.61E+03	1.43E+02
β_3	5.37E+03	6.02E+03	1.11E+03
β_4	-1.02E+03	-1.91E+03	6.87E+03
β_5	2.04E+03	1.81E+03	1.51E+02
β_6	-1.28E+04	-1.54E+04	-6.38E+02
β_7	5.23E+02	-3.06E+01	-1.74E+03
β_8	-1.90E+02	7.05E+01	-4.89E+03
β_9	-5.99E+02	2.82E+02	-9.34E+01
β_{10}	3.23E+03	3.33E+03	3.34E+03
β_{11}	-5.18E+02	-7.84E+02	-1.25E+03
β_{12}	-1.11E+03	-7.55E+01	1.71E+01
β_{13}	-2.56E+04	-2.82E+04	-2.90E+04
β_{14}	6.80E+03	5.86E+03	1.64E+04
β_{15}	1.38E+03	1.21E+03	1.10E+03
β_{16}	6.56E+04	6.39E+04	7.88E+04
β_{17}	3.36E+03	-2.59E+03	1.46E+03
β_{18}	-1.60E+04	-6.50E+02	-2.21E+04
β_{19}	-2.87E+03	-2.25E+03	-5.62E+03

Following the same method in Trial 1 (the coefficients in Table 24 and equations 19-21), a group of optimized points were found. Table 25 below shows the grouping of optimized points with varying weight values for CCC sampling. Similar to Trial 1, the point closest to the desired optimum will be analyzed further.

Table 25: Trial 2 CCC optimized points data

w_1	w_2	σ (ksi)	ε ($\mu\text{V/V}$)	σ/σ_0	$(\varepsilon-1700)/\varepsilon_0$	Distance from ideal point
1	0	239.2	1770.1	1.0261	0.0401	1.0269
0.9	0.1	239.1	1776.5	1.0259	0.0437	1.0269
0.8	0.2	238.9	1786.2	1.0249	0.0493	1.0261
0.7	0.3	238.1	1802.8	1.0216	0.0588	1.0233
0.6	0.4	235.3	1840.4	1.0095	0.0803	1.0127
0.5	0.5	-205.0	5076.6	-0.8794	1.9320	2.1228
0.4	0.6	167.0	2241.8	0.7164	0.3100	0.7806
0.3	0.7	-7261.7	24685.2	-31.1526	13.1517	33.8149
0.2	0.8	155.4	1800.1	0.6667	0.0573	0.6691
0.1	0.9	210.1	1718.8	0.9012	0.0108	0.9013
0	1	223.7	1712.6	0.9596	0.0072	0.9596

The point where $w_1 = 0.3$ results in a distance from the optimal point of 33.81, which is notably larger than the other distances. This abnormality occurred most likely due to the extreme x_1 and x_3 values as the optimal point, for $x_1 = 1069.1\%$ and $x_3 = 1314.1\%$ of its original dimension. These extreme variable values led to extreme stress and gauge reading values, resulting in a large distance from the ideal point. This point displays that there is a weakness to the objective function. When the stress value is projected to be negative at an optimized point, it can be cancelled with the positive gauge reading and the objective function becomes low even though it provides a large distance away from the idealized point. Of the eleven points found from CCC sampling in Trial 2, two cases ($w_1 = 0.5$ and 0.3) have negative stress output and excessive gauge reading and they are excluded for further analysis. When analyzing the other distances of optimized points to the desired point, the shortest distance occurred when $w_1 = 0.2$ and $w_2 = 0.8$. However, $x_1 = 178.3\%$ of its original dimension at this point, which lies outside the bounds ($34.9\% < x_1 < 174.5\%$, Section 3.1), so the next closest point was selected, which occurred when $w_1 = 0.4$ and $w_2 = 0.6$. At this location, $x_1 = -33.7\%$, which also lies outside the bounds. The next closest point was selected again, which occurred when $w_1 = 0.1$ and $w_2 = 0.9$. The optimized point's variables are as follows: $x_1 = 136.8\%$, $x_2 = 98.3\%$, and $x_3 = 119.4\%$ of the Trial 2 center point. This point was then tested in an FEA with a 20,000in-lb roll moment applied to compare the expected model value to the actual FEA value as shown in Table 26.

Table 26: Trial 2 – CCC optimized point output comparison

	<i>Equation</i>	<i>FEA</i>
<i>Stress (ksi)</i>	210.1	248.2
<i>Gauge reading ($\mu V/V$)</i>	1718.8	1674.6

The stress model had a larger error than the CCF and BB stress models in Trial 1, at 18.1%, but the gauge reading model only had an error of 2.57%.

This same process was done with CCF sampling. The table of optimized points can be seen in Table 27.

Table 27: Trial 2 CCF optimized points data

w_1	w_2	σ (ksi)	ϵ ($\mu V/V$)	σ/σ_0	$(\epsilon-1700)/\epsilon_0$	Distance from ideal point
1	0	237.7	1764.7	1.0196	0.0370	1.0202
0.9	0.1	237.6	1772.3	1.0193	0.0414	1.0202
0.8	0.2	237.3	1784.2	1.0181	0.0482	1.0192
0.7	0.3	236.4	1805.0	1.0140	0.0601	1.0157
0.6	0.4	233.1	1848.6	1.0000	0.0850	1.0036
0.5	0.5	217.7	1982.5	0.9341	0.1616	0.9480
0.4	0.6	-33.3	3370.7	-0.1427	0.9559	0.9665
0.3	0.7	-115.8	2644.1	-0.4967	0.5402	0.7339
0.2	0.8	185.7	1752.6	0.7968	0.0301	0.7974
0.1	0.9	214.6	1710.4	0.9208	0.0059	0.9208
0	1	223.2	1706.4	0.9576	0.0037	0.9576

Similar to the CCC Trial 2 model, the point with the least distance to the idealized point, where $w_1 = 0.3$ and $w_2 = 0.7$, contains a variable outside the bounds. In this case, $x_3 = 569.8\%$ of its original dimension, and therefore was too high a value ($8.33\% < x_3 < 433.3\%$, Section 3.1). Therefore, the next available point was selected as the best point, where $w_1 = 0.2$ and $w_2 = 0.8$. This point's variables are as follows: $x_1 = 119.0\%$, $x_2 = 111.1\%$, and $x_3 = 128.1\%$ of the Trial 2 center point. These variables were then applied to the model and tested in an FEA to compare the expected and actual stress and gauge reading values. This comparison is shown in Table 28.

Table 28: Trial 2 – CCF optimized point output comparison

	<i>Equation</i>	<i>FEA</i>
<i>Stress (ksi)</i>	185.7	234.6
<i>Gauge reading ($\mu V/V$)</i>	1752.6	1604.7

The CCF stress model had a smaller error than the CCC stress model at 2.63%, but the CCF gauge reading model had a slightly larger error than the CCC gauge reading model at 8.43%.

Finally, the BB data was analyzed in the same method. Table 29 displays the optimized points found from the BB coefficients at varying weight values.

Table 29: Trial 2 BB optimized points data

w_1	w_2	σ (ksi)	ε ($\mu V/V$)	σ/σ_0	$(\varepsilon-1700)/\varepsilon_0$	Distance from ideal point
1	0	228.5	2412.5	0.9801	0.4077	1.0615
0.9	0.1	227.5	2457.8	0.9758	0.4336	1.0678
0.8	0.2	177.3	4267.4	0.7608	1.4690	1.6543
0.7	0.3	-538.4	13521.5	-2.3099	6.7640	7.1476
0.6	0.4	168.5	2166.7	0.7229	0.2670	0.7706
0.5	0.5	204.4	1819.2	0.8769	0.0682	0.8796
0.4	0.6	216.0	1745.7	0.9266	0.0262	0.9270
0.3	0.7	221.9	1721.2	0.9520	0.0121	0.9521
0.2	0.8	225.7	1711.5	0.9683	0.0066	0.9684
0.1	0.9	228.6	1707.6	0.9806	0.0044	0.9806
0	1	231.2	1706.6	0.9918	0.0038	0.9918

The first point with the lowest distances to the idealized point, $w_1 = 0.6$, contained variables that lied outside the bounds, for $x_2 = 994.4\%$ of its original dimension and $x_3 = 484.8\%$ of its original dimension. Therefore, the next available point was selected as the best point, where $w_1 = 0.5$ and $w_2 = 0.5$. This point also contains variables outside the boundary, for $x_2 = 823.4\%$. The next best point was selected, where $w_1 = 0.4$ and $w_2 = 0.6$. This point's variables are as follows: $x_1 = 115.5\%$, $x_2 = 142.6\%$, and $x_3 = 119.5\%$ of the Trial 2 center point. These variables were then applied to the model and tested in an FEA to compare the expected and actual stress and gauge reading values. This comparison is shown in Table 30. The error for the BB stress model was in-between that of the CCC and CCF models at 12.7%. The gauge reading model error was also low at 4.02%.

Table 30: Trial 2 – BB optimized point output comparison

	Equation	FEA
Stress (ksi)	216.0	243.5
Gauge reading ($\mu V/V$)	1745.7	1675.5

A plot of the normalized stress and gauge reading for CCC, CCF, and BB sampling for Trial 2 can be shown below in Figure 30. Each sampling technique resulted in optimized points that are closer to the ideal point than Trial 2, but the variance is larger, as seen by the few outliers with



optimized point due to its design being close to ideal with both the stress and gauge reading value.

Table 31: Trial 2 best points stress and gauge reading FEA values

	CCC	CCF	BB
Stress (ksi)	248.2	234.6	243.5
Gauge reading ($\mu V/V$)	1674.6	1604.7	1675.5

To further show how Trial 2 had a better, more optimized result from Trial 1, Figure 31 displays a plot comparing the actual stress and gauge reading values of BB sampling from Trials 1 and 2. The plot shows that the gauge reading values are remarkably lower in Trial 2, centering around the ideal $1700\mu V/V$ point, whereas Trial 1 centers closer to $3300\mu V/V$. The stress values are also considerably lower and less varied in Trial 2, mostly laying between 200-250ksi, lower than Trial 1's stress values of 270-400ksi.

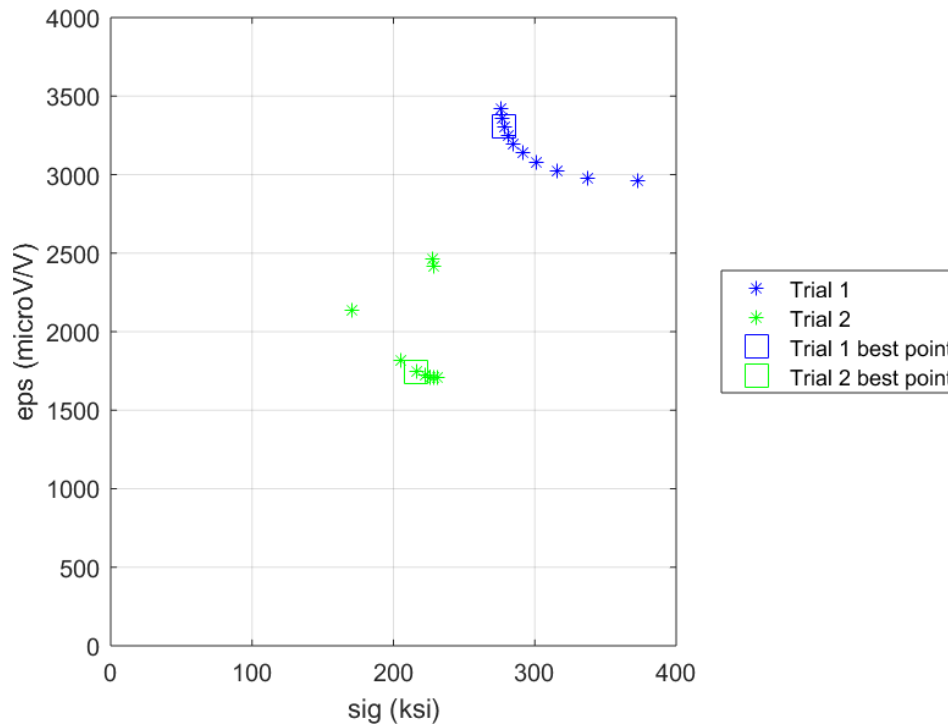


Figure 31: Stress and gauge reading values for Trial 1 and 2 BB sampling

Although the gauge reading values have reached satisfactory levels, the stress levels remain higher than not only the desired 156.6ksi stress value, but also the 235ksi ultimate strength.

3.3.3 Final Regression – sum of least squares error

To see if there are any points more optimized than the ones found in Trial 2, a final, concentrated regression will be conducted using the sum of least squares error. This requires taking the sum of least squares error equation

$$RSS = \sum_{i=0}^N (y_i - f(x_i))^2 \quad (23)$$

where y_i is the i th value of the variable to be predicted, x_i is the i th variable, $f(x_i)$ is the function serving to predict y_i , and N is the number of variables. The y_i and x_i values must be known to complete this regression process, and a total of 10 points are required. Three of the points selected were the best optimized points from Trial 2, which were the optimized points resulting in Table 31 (points 1-3 in Table 32), and the fourth point was the midpoint of those three (point 4 in Table 32). Another six points were selected to be varied in a small range around the four current points (points 5-10 in Table 32), and the stress and gauge readings for each set of variables was recorded from an FEA. The y_i will take the form of:

$$y = \frac{\sigma(x)}{\sigma_0} + \frac{|\varepsilon(x) - 1700|}{\varepsilon_0} \quad (24)$$

Table 32 displays the stress, gauge reading, and y values for each point selected for the regression. The x variables are represented by percentages of the original dimension from Trial 1.

Table 32: Regression output data

x_1	x_2	x_3	σ (ksi)	ϵ ($\mu\text{V/V}$)	y
136.8%	457.6%	398.2%	248.2	1674.6	1.094072
119.0%	516.5%	427.0%	234.6	1604.7	1.076059
115.6%	663.6%	398.3%	243.5	1675.5	1.073107
123.8%	545.9%	407.8%	245.5	1705.2	1.07045
133.6%	621.4%	389.3%	250.1	1762.8	1.124332
130.0%	528.1%	386.7%	233.3	1709.6	1.019995
120.0%	465.1%	366.7%	235.1	1721.7	1.034939
128.0%	465.1%	383.3%	246.6	1730	1.089821
133.8%	552.3%	391.7%	243.4	1756.3	1.091379
148.3%	639.5%	425.0%	247.1	1677.6	1.087524

The function $f(x_i)$ will take the following form, which is based on equation 10:

$$f = \alpha_0 + \alpha_1 x_1 + \alpha_2 x_2 + \alpha_3 x_3 + \alpha_4 x_1^2 + \alpha_5 x_2^2 + \alpha_6 x_3^2 + \alpha_7 x_1 x_2 + \alpha_8 x_1 x_3 + \alpha_9 x_2 x_3 \quad (25)$$

The partial derivative of the sum of least squares error equation with respect to α_i will be taken and set equivalent to zero. This will result in 10 total equations with 10 unknown coefficient variables. Using a linear solution, the coefficients are found to be as shown in Table 33. The coefficients show that the relationships of x_1 , x_3 , x_1^2 and x_3^2 helped to improve the stress and gauge reading performance the most, which is due to the higher α_1 , α_3 , α_4 , and α_6 coefficients.

Table 33: Regression coefficients

α_0	16.6377
α_1	245.5152
α_2	-15.2139
α_3	-340.8064
α_4	-462.4688
α_5	6.6686
α_6	634.8864
α_7	-64.8780
α_8	-21.2853
α_9	102.4683

By optimizing the function shown in equation 22 with the previous coefficients, the following optimized point is found: $x_1 = 133.5\%$, $x_2 = 505.8\%$, and $x_3 = 395.1\%$ of the original dimension. The 6th point used as a sample in Table 32, where $x_1 = 130\%$, $x_2 = 528.1\%$, and $x_3 = 386.7\%$ of the original dimension, was found to have a slightly better result than the best optimized point from the regression. However, the variance between the two points is minimal, and due to the slight variance of FEA results, these two points can be treated as nearly identical, as the difference between the two points' dimensions fall below 0.005 inches, which is around manufacturing tolerance [26]. This point was tested in an FEA with a roll moment of 20,000in-lb and compared the expected values of stress and the gauge reading. This comparison is shown in Table 34. This is a large improvement from Trial 1 where the best point produced a stress value of 289.4ksi and a gauge reading of 3018.1 μ V/V.

Table 34: Regression optimized point output comparison

	<i>Equation</i>	<i>FEA</i>
<i>Stress (ksi)</i>	246.1	240.1
<i>Gauge reading (μV/V)</i>	1730.4	1715.3

This point is closer to the idealized point than the best point from Trial 2, which resulted from BB sampling. Therefore, this point is the most optimized point calculated thus far. It is unlikely that continuing optimization with the chosen variables will provide any further notable improvement. From Trial 2 to the regression, the stress value decreased by 1.39%, whereas the gauge reading value improved by 0.541%. Therefore, the best course of action is to select new design variables to further optimize this part, which is explained in Section 4.2.

4. Conclusion and future work

4.1 Conclusion

The most optimized point found in this study consists of the following variables in Table 35. This study shows that by making the roll cage stiffer by altering the flexures, the force balance assembly can withstand a larger roll moment.

Table 35: Optimized variables by the final regression model

<i>Variable</i>	<i>% of original dimension</i>
x_1	133.5%
x_2	505.8%
x_3	395.1%

Figure 32 displays the comparison between the original and updated roll cage flexures, and Figure 33 displays the comparison between the original and updated roll cage gauge location thickness.

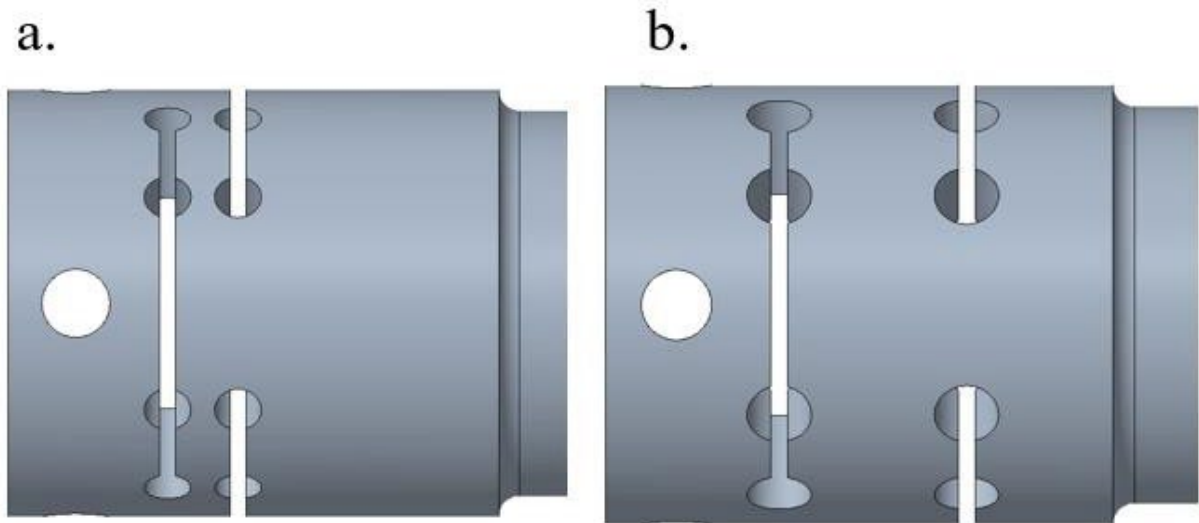


Figure 32: Forward end of roll cage flexures. (a) Original roll cage flexures. (b) Updated roll cage flexures

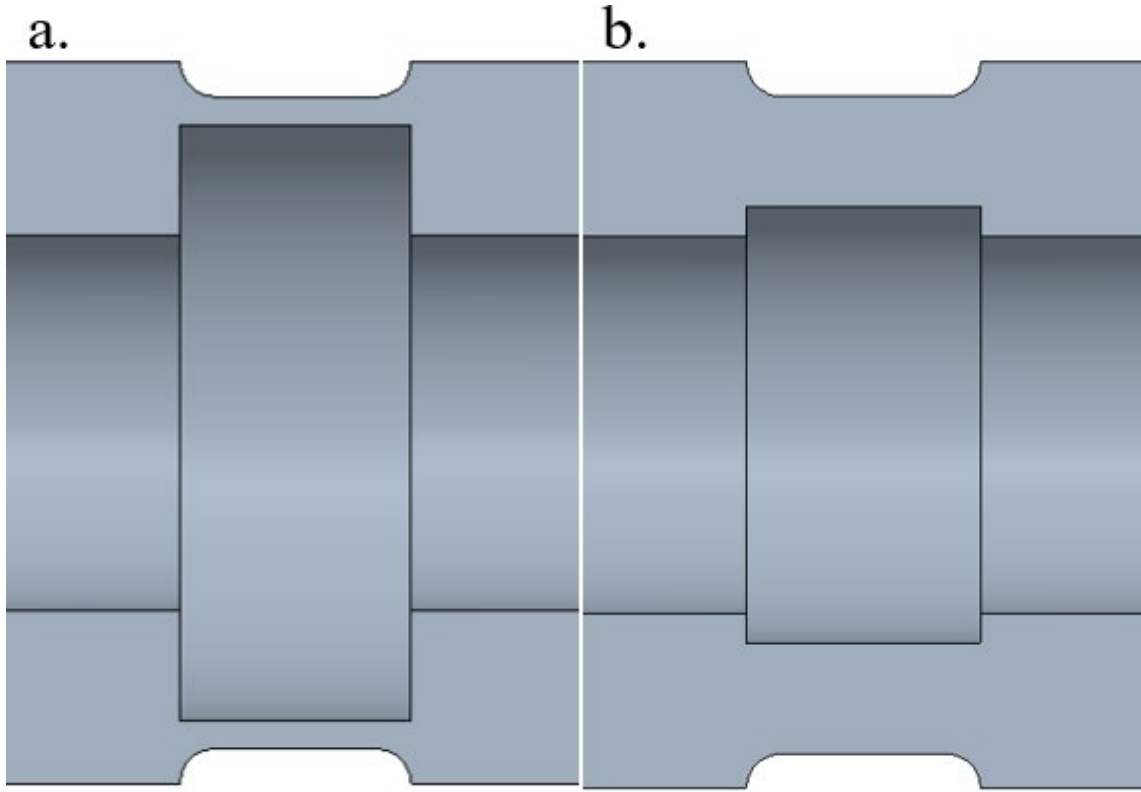


Figure 33: Cross-sectional view of roll cage gauge location. (a) Original roll cage gauge location. (b) Updated roll cage gauge location.

This point resulted from the regression study in Section 3.3.3. The gauge reading value at this point, $1715.3\mu\text{V/V}$, is satisfactory, as it is close to the desired $1700\mu\text{V/V}$ gauge reading that was found in calibration. However, the stress value, 240.1ksi , while an improvement from the 371ksi value that was recorded from the original model, is not at the desired 156.6ksi stress level, nor is it beneath the ultimate strength of 235ksi . More work will have to be done on the model in order to bring the maximum stress value down to a satisfactory level.

4.2 Future work

Further optimization must be conducted to further lower the stress value. It is unlikely that the model will produce a smaller maximum stress value than 240ksi with the current variable setup. Therefore, new variables to assist the stress must be selected. Some possible variable selections

include the radial distance between hole cutouts in the flexure, the cutout thickness in the flexure, and the shape of the hole cutouts (i.e., test how the model reacts if the circular hole cutouts are changed to ellipses). Figure 34 displays the radial distance between hole cutouts and the cutout thickness variables for clarity.

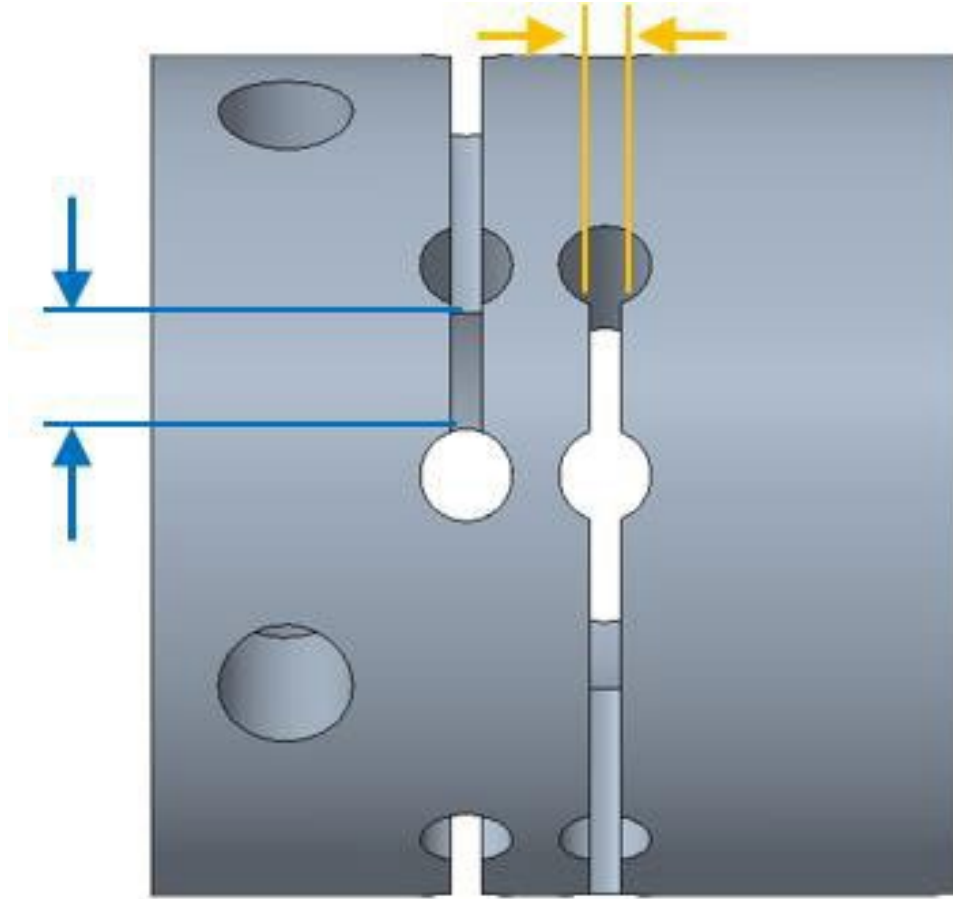


Figure 34: Radial distance between hole cutouts in roll cage flexure (blue). Cutout thickness in roll cage flexure (yellow)

The force balance may also experience a material change to increase the ultimate strength of the assembly, therefore raising the desired $\frac{2}{3}$ of ultimate strength stress limit. The new material would be 300 Maraging steel, for it is used in similar tools at NASA Langley Research Center. This material has an ultimate strength of 293ksi, making the desired limit 195.3ksi. The current

optimized balance has a maximum von Mises stress value of 240.1ksi, which does not fit the 195.3ksi criteria of the new material, but is below the ultimate strength, so the piece is not expected to fail.

Once a new design is selected after the maximum stress is brought down to acceptable levels, a prototype must be created and tested at the 20,000in-lb rated roll moment to ensure the piece will not fail at that load and compare the true stress and gauge reading values to the theoretical finite element model.

5. References

- [1] D. Burns, P. Parker, “Additively Manufactured Wind-Tunnel Balance,” *Aerospace Research Central*, vol. 57, no. 5, 2020.
- [2] M. Feero, A. Naguib, M. Koochesfahani, “Single-component force balance for the measurement of low-magnitude mean aerodynamic loads,” *Measurement Science and Technology*, vol. 30, no. 11, 2019.
- [3] C. Tropea, A. Yarin, J. F. Foss (Eds.), *Springer Handbook of Experimental Fluid Mechanics*, 2007.
- [4] R. P. Davie, 1958, *Temperature Compensated Force Balance*, 2844027.
- [5] M. Robinson, J. M. Schramm, K. Hannemann, “Investigation into Internal and External Force Balance Configurations for Short Duration Wind Tunnels,” *Notes on Numerical Fluid Mechanics and Multidisciplinary Design (NNFM)*, vol 96, 2007
- [6] B. F. R Ewald, “Multi-component force balances for conventional and cryogenic wind tunnels,” *Measurement Science and Technology*, vol. 11, no. 6, 2000.
- [7] S. Post, M. Morris, “Force Balance Design for Educational Wind Tunnels,” *Peoria, [IL]: Bradley University, Dept. of Mechanical Engineering*, 2010.
- [8] I. B. Tintoré, “Design of a Three-axis Wind Tunnel Force Balance,” *Zagreb, [HR]: University of Zagreb, Faculty of Transport and Traffic Sciences*, 2018.
- [9] Đ. Vuković, D. Damljanić, “Evaluation of a force balance with semiconductor strain gages in wind tunnel tests of the HB-2 standard model,” *Proceedings of the Institution of Mechanical Engineers, Part G: Journal of Aerospace Engineering*, vol. 229, no. 12, pp. 2272-2281, 2015.

- [10] P. Vadassery, "Design, calibration and testing of a force balance for a hypersonic shock tunnel," *Arlington, [TX]: University of Texas at Arlington, Dept. of Aerospace Engineering*, 2012.
- [11] G. Kalaiarassan, Krishan, M. Somanadh, C. Thirumalai, M. S. Kumar, "One-Dimension Force Balance System for Hypersonic Vehicle an experimental and Fuzzy Prediction Approach," *Materials Today: Proceedings*, vol. 5, no. 5, part 2, 2018,
- [12] M. W. Kniskern, "Analysis of a six-component, flow-through, strain-gage, force balance used for hypersonic wind tunnel models with scramjet exhaust flow simulation [microform]," *Raleigh, [NC]: North Carolina State University, Dept. of Mechanical and Aerospace Engineering*, 1990.
- [13] C. Abe, "Aerodynamic force and moment balance, design, fabrication, and testing for use in low Reynolds flow applications," *Rochester Institute of Technology*, 2003.
- [14] A. Aboelezz, Y. Elqudsi, M. Hassanalian, A. Desoki, "Wind tunnel calibration, corrections and experimental validation for fixed-wing micro air vehicles measurements," *Aviation*, vol. 23, no. 4, pp. 104-113, 2019.
- [15] D. Burns, K. Toro, P. Parker, S. M. Rivers, H. Quix, M. Wright, "Evaluation of Cryogenic Force Balance Calibration Methodologies Relative to Wind Tunnel Results," *Journal of Aircraft*, vol. 56, no. 4, pp. 1398-1406, 2019.
- [16] Y. Wang, Y. Liu, C. Luo, Z. Jiang, "Force measurement using strain-gauge balance in shock tunnel with long test duration," *Review of Scientific Instruments*, vol. 87, no. 5, pp. 55-108, 2016.

- [17] A. Xu, Z. Xie, M. Gu, J. Wu, "A new method for dynamic parameters identification of a model-balance system in high-frequency force-balance wind tunnel tests," *Journal of Vibroengineering*, vol. 17, no. 5, pp. 2609-2623, 2015.
- [18] R. Zhao, A. Xu, W. Sun, X. Lan, "Model shape correction method for high-frequency force balance technique." *Journal of Vibroengineering*, vol. 19, no. 3, pp. 1665-1679, 2017.
- [19] L. Zhang, Y. Wang, Z. Xie, "Three-dimensional coupled wind-induced vibration calculation method for super high-rise buildings based on high-frequency force balance technology," *Structural Design of Tall and Special Buildings*, vol. 29, no. 12, pp. 1772-1786, 2020.
- [20] R. J. Jeracki, "Model Engine Performance Measurement from Force Balance Instrumentation," *National Aeronautics and Space Administration, 34th Joint Propulsion Conference and Exhibit*, 1998.
- [21] M. Gonzalez, J. M. Ezquerro, V. Lapuerta, A. Laveron, J. Rodriguez, "Components of a Wind Tunnel Balance: Design and Calibration," *Wind Tunnels and Experimental Fluid Dynamics Research*, vol. 1, pp. 115-134, 2011.
- [22] C. X. Li, G. Y. Gu, M. J. Yang, L. M. Zhu, "Design, analysis and testing of a parallel-kinematic high-bandwidth SY nan positioning stage," *Review of Scientific Instruments*, vol. 84, no. 12, 2013.
- [23] D. Kai, H. Sugiura, A. Tezuka, "Magnetic Suspension and Balance System of High-Subsonic Wind Tunnel," *Aerospace Research Central*, vol. 57, no. 6, 2019.
- [24] L. B. S. Alves, M. Gabaldo, L. S. Dutra, J. E. M. Barros, "Wind Tunnel Balance," *26th SAE BRASIL International Congress and Display*, 2017.

- [25] H. H. Bennett, "Finite Element Analysis of a Wind Tunnel Balance" Internal NASA report: unpublished, 2018.
- [26] M. A. Wolf, "Final stress analysis of the force balance", Internal NASA report: unpublished, 1974.
- [27] A. Y. Aydar, "Utilization of Response Surface Methodology in Optimization of Extraction of Plant Materials," *Statistical Approaches with Emphasis on Design of Experiments Applied to Chemical Processes*, pp. 157-169, 2018.
- [28] Y. W. Liu, F. Moses, "A sequential response surface method and its application in the reliability analysis of aircraft structural systems," *Structural Safety*, vol 16. no. 1-2, pp. 39-46, 1994.
- [29] Z. Ren, W. Li, R. Billinton, W. Yan, "Probabilistic Power Flow Analysis Based on the Stochastic Response Surface Method," *IEEE Transactions on Power Systems*, vol. 31, no. 3, pp. 2307-2315, 2016.
- [30] W. Zhao, F. Fan, W. Wang, "Non-linear partial least squares response surface method for structural reliability analysis," *Reliability Engineering and System Safety*, vol. 161, pp. 69-77, 2017.
- [31] W. J. Hill, W. G. Hunter, "A Review of Response Surface Methodology: A Literature Survey," *Technometrics*, vol. 8, no. 4, 1966.
- [32] S. K. Behera, H. Meena, S. Chakraborty, B. C. Meikap, "Application of response surface methodology (RSM) for optimization of leaching parameters for ash reduction from low-grade coal," *International Journal of Mining Science and Technology*, vol. 28, no. 4, pp. 621-629, 2018.

- [33] K. Anwar, M. Said, M. Afizal, M. Amin, "Overview on the Response Surface Methodology (RSM) in Extraction Processes," *Journal of Applied Science and Process Engineering (JASPE)*, vol. 2, no. 1, 2015.
- [34] G. G. Wang, Z. Dong, P. Aitchison, "Adaptive Response Surface Method – A Global Optimization Scheme for Approximation-based Design Problems," *Engineering Optimization*, vol. 33, pp. 707-733. 2001.
- [35] B. Keshtegar, P. Hao, Y. Wang, Q. Hu, "An adaptive response surface method and Gaussian global-best harmony search algorithm for optimization of aircraft stiffened panels." *Applied Soft Computing*, vol. 66, pp. 196-207, 2018.
- [36] J. Tu, K. K. Choi, Y. H. Park, "A new study on reliability-based design optimization," *Journal of Mechanical Design*, vol. 121, no. 4, pp. 557-564, 1999.
- [37] A. Chiralaksanakul, S. Mahadevan, "First-order approximation methods in reliability-based design optimization," *Journal of Mechanical Design*, vol. 127, no. 5, pp. 851-857, 2004.
- [38] Z. Wang, Y. Zhang, Y. Song, "A modified conjugate gradient approach for reliability-based design optimization," *IEEE Access*, vol. 8, pp. 16742-16749, 2020.
- [39] X. L. Yin, W. Chen, "Enhanced sequential optimization and reliability assessment method for probabilistic optimization with varying design variance," *Structure and Infrastructure Engineering*, vol. 2, no. 3-4, pp. 261-275, 2006.
- [40] X. P. Du, W. Chen, "Sequential optimization and reliability assessment method for efficient probabilistic design," *Journal of Mechanical Design*, vol. 126, no. 2, pp. 225-233, 2004.

- [41] J. Liang, Z. P. Mourelatos, E. Nikolaidis, "A single-loop approach for system reliability-based design optimization," *ASME, Journal of Mechanical Design*, pp. 1215-1224, 2007.
- [42] Y. Shi, Z. Lu, Z. Huang, "Time-dependent reliability-based design optimization with probabilistic and interval uncertainties," *Applied Mathematical Modelling*, vol. 80, pp. 268-289, 2020.
- [43] P. Fang, Z. Wen, "Single-loop method for reliability-based design optimization of turbine blades with poor information," *Prognostics and System Health Management Conference*, pp. 1-5, 2019.
- [44] M. Qin, H. Zhang, G. Zhou, H. Wang, C. Zhang, P. He, "Reliability design optimization method based on information reconstruction Kriging model," *International Conference on Sensing, Diagnostics, Prognostics, and Control*, pp. 1062-1068, 2019.
- [45] Y. Wang, X. Ma, H. Zhang, D. Hong, "A combined logistic regression and learning Kriging method for reliability-based design optimization," *International Conference on Sensing, Diagnostics, Prognostics, and Control*, pp. 1075-1084, 2019.
- [46] J. Jafari-Asl, M. E. A. Ben Seghier, S. Ohadi, P. van Gelder, "Efficient method using Whale Optimization Algorithm for reliability-based design optimization of labyrinth spillway," *Applied Soft Computing Journal*, vol. 101, 2021.
- [47] Z. L. Huang, C. Jiang, X. M. Li, X. P. Wei, T. Fang, X. Han, "A Single-Loop Approach for Time-Variant Reliability-Based Design Optimization," *IEEE Transactions on Reliability*, vol. 66, no. 3, pp. 651-661, 2017.

- [48] J. Mun, J. Lim, Y. Kwak, B. Kang, K. K. Choi, D. Kim, "Reliability-Based Design Optimization of a Permanent Magnet Motor Under Manufacturing Tolerance and Temperature Fluctuation," *IEEE Transactions on Magnetics*, vol. 57, no. 6, pp. 1-4, 2021.
- [49] H. Zhao, S. Li, B. Chen, "The Reliability-Based Design Optimization of considering Rock-Support Interaction for Rock Tunnels," *Advances in Civil Engineering*, pp. 1-13, 2021.
- [50] X. Liu, R. Wang, D. Hu, J. Mao, G. Chen, "Reliability-based design optimization approach for compressor disc with multiple correlated failure modes," *Aerospace Science and Technology*, vol. 110, 2021.
- [51] S. M. Baek, W. J. Lee, "Design method for radar absorbing structures using reliability-based design optimization of the composite material properties," *Composite Structures*, vol. 262, 2021.
- [52] P. Rong, Z. Xiaotian, S. Qing, "Product design optimization with simulation-based reliability analysis," *International Conference on Quality, Reliability, Risk, Maintenance, and Safety Engineering*, 2012.
- [53] J. Chen, W. Lu, W. Hu, Z. Liu, Y. Zhang, J. Tan, "Hybrid Reliability-Based Design Optimization of Complex Structures with Random and Interval Uncertainties based on ASS-HRA," *IEEE Access*, vol. 7, pp. 87097-87109, 2019.
- [54] K. C. Foye, R. Salgado, B. Scott, "Assessment of Variable Uncertainties for Reliability-Based Design of Foundations," *Journal of Geotechnical and Geoenvironmental Engineering*, vol. 132, no. 9, pp. 1197-1207, 2006.

- [55] S. Yu, “Reliability-Based Design Optimization for the knee Joint of the Lower Extremity Exoskeleton,” *Annual Reliability and Maintainability Symposium*, pp. 1-5, 2018.
- [56] K. Cheng, Z. Lu, S. Xiao, S. Oladyshkin, W. Nowak, “Resampling method for reliability-based design optimization based on thermodynamic integration and parallel tempering,” *Mechanical Systems and Signal Processing*, vol. 156, 2021.
- [57] “Force Balance Design,” Internal NASA report: unpublished. 2009.
- [58] “Products: Creo.” [Online]. Available: <https://www.ptc.com/en/products/creo>
- [59] “Response Surface Designs.” [Online]. Available: <https://www.itl.nist.gov/div898/handbook/pri/section3/pri336.htm>
- [60] “Force balance calibration report,” Internal NASA report, unpublished, 2008.
- [61] A. T. Eshghi, S. Lee, “Adaptive improved response surface method for reliability-based design optimization,” *Engineering Optimization*, vol. 51, no. 12, pp. 1-19, 2019.

